J. Fluid Mech. (1997), *vol.* 346, *pp.* 117–148. Printed in the United Kingdom

Buoyancy-driven coalescence of slightly deformable drops

By MICHAEL A. ROTHER, ALEXANDER Z. ZINCHENKO AND ROBERT H. DAVIS†

Department of Chemical Engineering, University of Colorado, Boulder, CO 80309-0424, USA

(Received 13 November 1996 and in revised form 31 March 1997)

The simultaneous effect of small deformation and short-range van der Waals attraction on the coalescence efficiency of two different-sized slowly sedimenting drops is considered. For spherical drops, it has been shown previously that the tangential mobility of drop surfaces makes collision possible even without van der Waals attraction; on the other hand, even a small amount of deformation precludes drops from coming into contact unless van der Waals attraction is accounted for. In the present work, the conditions are delineated when these two small-scale factors, acting in opposite directions, have a considerable combined effect on the coalescence efficiency. The problem is solved by matched asymptotic expansions valid for small capillary numbers (Ca). The outer solution, for two spherical drops moving in apparent contact without van der Waals attraction, determines the contact force as a function of time. This force is used as the driving force for the inner solution of the relevant integro-differential thin-film equations (coupling the flow in the small-gap region to that inside the drops) to determine whether coalescence occurs during the apparent contact motion. The initial gap profile for the inner solution is provided by matching with the outer trajectory for spherical drops approaching contact.

The analysis shows that, for $Ca \ll 1$, the near-contact deformation is mainly axisymmetric, greatly simplifying the inner solution; nevertheless, determination of the critical horizontal offsets leading to coalescence and the parametric analysis are computationally very intensive. To facilitate these tasks, a substantially new, highly efficient, and absolutely stable numerical method for solving stiff thin-film equations is developed. Unlike for spherical drops, when the upstream intersection area is a circle, the existence of a second coalescence zone for deformable drops is found over much of the parameter space. Results are mapped out for a range of four dimensionless parameters (capillary number, size and drop-to-medium viscosity ratios, dimensionless Hamaker parameter). As a physical application, predicted coalescence efficiencies are shown for a system of ethyl salicylate drops in diethylene glycol.

The present solution extends the range of drop sizes where the coalescence efficiencies are known theoretically and can be used in drop population dynamics. Comparison with full three-dimensional boundary-integral calculations for deformable drops without van der Waals attraction is also made to demonstrate that, when the drop-to-medium viscosity ratio is of the order of unity, the present asymptotic approach is valid in a wide range of small and moderately small capillary numbers.

† Author to whom correspondence should be addressed.

1. Introduction

Coalescence phenomena are significant not only in nature, as in raindrop formation, but also in industry, as in liquid–liquid extraction and flotation. Knowledge of collision rates for such processes allows prediction of drop growth and phase separation on the macroscopic level through the use of population dynamics (Reddy, Melik & Fogler 1981; Rogers & Davis 1990; Wang & Davis 1993, 1995; Zhang, Wang & Davis 1993).

Previous calculations for the collision rate of spherical drops in Stokes flow have been based on the exact bipolar coordinate solutions for the motion along and normal to the line of centres (Haber, Hestroni & Solan 1973; Rushton & Davies 1978; Zinchenko 1980) and lubrication asymptotics (Zinchenko 1978, 1982; Davis, Schonberg & Rallison 1989). Since the hydrodynamic resistance between two spherical drops contains an integrable singularity, collision is possible even in the absence of van der Waals forces. Thus, Zinchenko (1982) was able to determine the collision rate of two settling non-Brownian drops without colloidal forces. Subsequently, Zhang & Davis (1991) included van der Waals attraction and considered Brownian drops as well. Having obtained a bipolar coordinate solution for arbitrarily sized freely suspended drops in a shear flow, Wang, Zinchenko & Davis (1994) performed calculations for the collision rate, both with and without van der Waals forces. For extreme drop size ratios, the image solutions of Fuentes, Kim & Jeffrey (1988, 1989) may turn out to be more suitable, but the problem remains unstudied. The case of two semi-Brownian drops or solid spheres was analysed recently by Zinchenko & Davis (1994, 1995) for buoyancy-driven and shear flow.

The above studies neglected the effects of drop deformation on film drainage, despite a considerable body of research pertaining to thinning rates and rupture between deformable interfaces (Hahn, Chen & Slattery 1985; Jones & Wilson 1978; Yiantsios & Higgins 1989; Chesters 1991). The work of Yiantsios & Davis (1990, 1991) is of particular relevance here. They coupled the lubrication flow in the gap to the internal flow within the drops by a local boundary integral approach and showed that, for the case of drops moving along their line of centres, an infinite time is required for coalescence in the absence of van der Waals forces. Thus, if deformation becomes important before van der Waals attraction is dominant, small deformation can significantly reduce the collision rate from its value for spherical drops. Moreover, an important question arises about the range of validity of the collision rate calculations made for non-deformable drops.

Previous experimental work supports the idea that small deformations inhibit coalescence. Zhang, Davis & Ruth (1993) found that, when the initial horizontal offset between two drops under low-Reynolds-number and low-capillary-number conditions was small enough for spherical drops to coalesce, the drops nevertheless passed by one another with only rare coalescence. In addition, symmetry in the relative trajectories was lost – a phenomenon which could be due to deformation.

Manga & Stone (1993, 1995), however, found that deformation promotes coalescence for moderate and large capillary numbers. For the buoyancy-driven motion of air bubbles in corn syrup, they observed that a larger bubble passing by a smaller one can 'suck' the smaller bubble toward it due to deformation. They also presented experimental evidence that the collision efficiency when deformation is finite might surpass that predicted by the Smoluchowski model. Presumably, the very small viscosity ratio plays a crucial role in these experiments by acting (i) to increase the bubble tendency to migrate laterally and align, (ii) to decrease the bubble tendency to break up prematurely (Rallison 1984; Bentley & Leal 1986), and (iii) to decrease

the lubrication resistance of the film at the latest stage. Unlike in Manga & Stone's experiments, the case of moderate drop-to-medium viscosity ratios is considered in the present work.

The goal of the present work is to calculate collision rates in a dilute dispersion of slightly deformable drops in buoyancy-driven flow. In §2, the problem and basic assumptions are outlined. In §3, the general approach and governing equations are presented. The numerical technique employed in solving the thin-film equations is described and compared with previous methods in §4, while full three-dimensional boundary integral calculations are presented in §5 to justify underlying hypotheses and as a means of evaluating the accuracy of the asymptotic approach. Section 6 contains results which indicate the existence of two coalescence zones for slightly deformable drops over much of the parameter space. In addition, parametric analysis of collision efficiencies is made, and specific collision efficiencies for ethyl salicylate drops in diethylene glycol are determined.

2. Formulation of the problem

We consider the motion of two drops immersed in an immiscible and unbounded fluid under the influence of gravity at low Reynolds numbers. The surface tension is assumed to be sufficiently large that the drop deformation can be considered as a small (but singular) perturbation. The viscosity of the drop phase is assumed to be of the same order of magnitude as that of the surrounding medium, and the interfaces are free of surfactants. In addition, electrostatic repulsion is neglected, which is appropriate for unstable systems with rapid coalescence. The drops have undeformed radii a_1 and a_2, with size ratio $k = a_1/a_2 < 1$, and both have density ρ' and viscosity μ'. Gravity acts vertically downward, and so the drops sediment downwards if their density is greater than that of the matrix fluid, ρ_e. The viscosity of the surrounding fluid is μ_e, and $\hat{\mu} = \mu'/\mu_e$ is the viscosity ratio.

The collision rate between drops of radii a_1 and a_2 per unit volume is

$$J_{12} = n_1 n_2 \, |V_1^\infty - V_2^\infty| \, \pi (a_1 + a_2)^2 E_{12}, \tag{2.1}$$

where n_1 and n_2 are the corresponding number densities, E_{12} is the collision efficiency (which accounts for non-rectilinear motion due to hydrodynamic and interdroplet interactions), and the isolated drop velocities are given by

$$V_i^\infty = \frac{2}{9} \frac{(\rho' - \rho_e) g}{\mu_e} \left(\frac{\hat{\mu} + 1}{\hat{\mu} + \frac{2}{3}} \right) a_i^2, \quad i = 1, 2. \tag{2.2}$$

In determining the collision efficiency, it is necessary to find the upstream intersection area leading to coalescence relative to $\pi(a_1 + a_2)^2$. At infinite separation, the horizontal offset between the drop centres is d_∞. For simple cases, the collision efficiency is $E_{12} = [d_\infty^*/(a_1 + a_2)]^2$, where d_∞^* is the critical horizontal offset separating colliding and non-colliding trajectories. In previous work (Zhang & Davis 1991), finite collision efficiencies were obtained without including the effects of deformation and van der Waals attraction. Yiantsios & Davis (1990, 1991), however, showed that coalescence cannot take place when small deformation occurs in the absence of attractive molecular forces. Thus, it is of particular interest to investigate how small deformation and short-range van der Waals forces, both small-scale effects, make the collision efficiency differ from that for spheres without attractive forces. Our purpose is to study the collision efficiency as a function of four dimensionless parameters: k, $\hat{\mu}$,

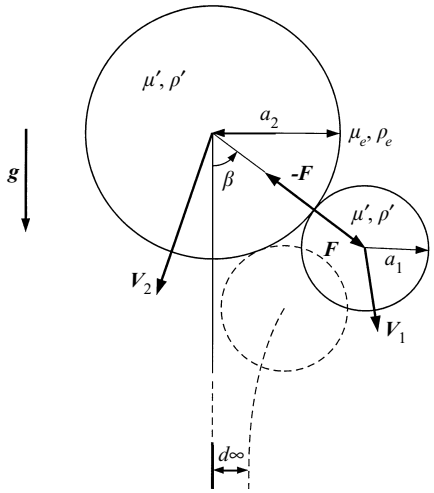

FIGURE 1. Definition sketch for two spherical drops in apparent contact.

δ (a dimensionless Hamaker parameter defined in (3.21)), and the capillary number:

$$Ca = \frac{\mu_e |V_1^\infty - V_2^\infty|}{\sigma}, \tag{2.3}$$

where σ is the constant interfacial tension.

3. General method of the solution

3.1. *Outer region*

When the capillary number is sufficiently small, significant deformation of the drops will be confined to the small-gap region in the vicinity of near contact. On the length scale of the drop size, the two drops can be considered as fluid spheres, which come into contact without van der Waals attraction at some initial value β_0 of the angle β between the line of centres and the vertical (see figure 1). Viewed from this outer solution, the drops appear to move in contact, until they either coalesce or separate. However, on the deformation length scale, there is a small non-uniform gap between the drops that evolves under the action of van der Waals and hydrodynamic forces. When β_0 is small enough, van der Waals forces have enough time to pull the drops together and cause the film rupture. If β_0 is increased, we expect a critical value β_c to exist, beyond which the drops will separate and pass by one another. The problem is reduced to determining the critical angle β_c, because the critical offset parameter, d_∞^*, and the coalescence efficiency, $E_{12} = [d_\infty^*/(a_1+a_2)]^2$, can be found simply by backward integration of the governing equations for two spherical drops in the absence of van der Waals attraction (Zinchenko 1982), starting from $\beta = \beta_c$.

From the linearity of the Stokes equations and the formulation of Zinchenko (1982), the forces acting on two spherical drops in apparent contact can be written as

$$\boldsymbol{F}_1 = -6\pi\mu_e a_1 \left[\Lambda_{12}\boldsymbol{V} + T_{11}(\boldsymbol{V}_1 - \boldsymbol{V}_2)^\perp + T_{12}\boldsymbol{V}_2^\perp\right] + \boldsymbol{F}, \tag{3.1a}$$

$$\boldsymbol{F}_2 = -6\pi\mu_e a_2 \left[\Lambda_{22}\boldsymbol{V} + T_{21}(\boldsymbol{V}_2 - \boldsymbol{V}_1)^\perp + T_{22}\boldsymbol{V}_2^\perp\right] - \boldsymbol{F}, \tag{3.1b}$$

where $\boldsymbol{V} = \boldsymbol{V}_1^\parallel = \boldsymbol{V}_2^\parallel$ is the common velocity of the drops along the line of centres, $\perp$ marks components perpendicular to the line of centres, and $\boldsymbol{F}$ and $-\boldsymbol{F}$ are the equal

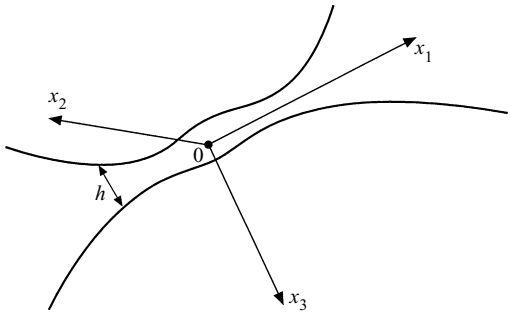

FIGURE 2. Definition sketch for inner region, where small deformation has occurred.

and opposite contact forces acting between the two drops along their line of centres. Here, $\boldsymbol{V}_1$ and $\boldsymbol{V}_2$ are the velocities of the geometrical centers of spherical drops. The hydrodynamic resistance coefficients Λ_{12} and Λ_{22} for an aggregate of two touching spheres are given by Reed & Morrison (1974), and the T_{ij} values are given by the results of Zinchenko (1980) in the limit of zero gap.

The overall force balances, $\boldsymbol{F}_i + \frac{4}{3}\,\pi a_i^3 \Delta\rho \boldsymbol{g} = 0$, projected along the line of centres allow exclusion of $\boldsymbol{V}$ and give the expression for the magnitude of the contact force:

$$F = \frac{4}{3}\,\pi\,\frac{a_1 a_2\left(a_2^2\Lambda_{12} - a_1^2\Lambda_{22}\right)}{a_2\Lambda_{22} + a_1\Lambda_{12}}\,\Delta\rho g\cos\beta. \tag{3.2}$$

The overall force balances in the transverse direction normal to the line of centres give the equation for the relative tangential motion:

$$\frac{\mathrm{d}\beta}{\mathrm{d}t} = \kappa T\sin\beta, \tag{3.3}$$

where

$$\kappa = \frac{2}{9}\,\frac{\Delta\rho g a_2^2}{(a_1 + a_2)\mu_e}, \quad T = \frac{T_{12} - k^2 T_{22}}{T_{11}T_{22} + T_{21}T_{12}}, \tag{3.4}$$

which can be integrated to yield

$$\beta = 2\arctan\left[\tan\left(\tfrac{1}{2}\beta_0\right)\exp\left(\kappa T t\right)\right], \tag{3.5}$$

assuming $\beta = \beta_0$ at $t = 0$. Combining (3.2) and (3.5) gives the contact force as an explicit function of time. A key feture of the solution is that the small deformation in the region of near contact affects the rate of film drainage and relative motion along the line of centres, but does not affect the transverse relative motion normal to the line of centres for $Ca \ll 1$. Thus, (3.5) applies in the inner region as well.

3.2. *Inner region*

Although the drops appear to be in contact when viewed from the outer region, they are actually separated by a thin film which exhibits lubrication flow. The 'contact' force given by equations (3.2) and (3.5) is the driving force for the integro-differential system of the thin-film equations which couple the lubrication flow in the gap region to the internal flow within the drops. This force takes the form of a lubrication force arising from the dynamic pressure within the thin film. In the local Cartesian coordinate system (x_1, x_2, x_3) with the origin O at the point of contact of non-deformed spheres, and the x_3-axis along their line of centres (figure 2), these equations take the form

Normal stress balance

$$p - \frac{A}{6\pi h^3} = \sigma\left(\frac{1}{a_1} + \frac{1}{a_2}\right) - \frac{\sigma}{2}\,\nabla_S^2\, h, \tag{3.6}$$

Momentum balance

$$\boldsymbol{f} = -\tfrac{1}{2} h\,\nabla_S\, p, \tag{3.7}$$

Local boundary integral

$$\boldsymbol{u}(\boldsymbol{x}) = \frac{1}{4\pi\mu'}\int_{-\infty}^{\infty}\int_{-\infty}^{\infty}\left[\frac{\boldsymbol{f}(\boldsymbol{x}')}{r} + \frac{(\boldsymbol{f}(\boldsymbol{x}')\cdot\boldsymbol{r})\boldsymbol{r}}{r^3}\right]\,\mathrm{d}x_1\mathrm{d}x_2, \tag{3.8}$$

Mass continuity

$$\frac{\partial h}{\partial t} + \nabla_S\cdot[h(\boldsymbol{v}-\boldsymbol{v}_0)] = 0, \tag{3.9}$$

Integral force balance

$$\int_{-\infty}^{\infty}\int_{-\infty}^{\infty}\left(p - \frac{A}{6\pi h^3}\right)\,\mathrm{d}x_1\mathrm{d}x_2 = F(t), \tag{3.10}$$

where h, p, $\boldsymbol{f}$, and $\boldsymbol{v}$ depend on t, x_1 and x_2 and are, respectively, the film thickness, the dynamic pressure, the tangential stress exerted by the lubrication flow on the fluid inside the drops, and the fluid velocity in the film; $-A/6\pi h^3$ is the unretarded van der Waals disjoining pressure (Hamaker 1937) with effective Hamaker constant A; $\boldsymbol{v}_0$ is the velocity of the point of contact O of the two non-deformed spheres; $\boldsymbol{u} = \boldsymbol{v} - \boldsymbol{v}_{outer}$ is the velocity perturbation, where $\boldsymbol{v}_{outer}$ is the mutual fluid velocity from the outer solution at the point of contact O; subscript S denotes differential operations in the (x_1, x_2)-plane; $\boldsymbol{r} = \boldsymbol{x}' - \boldsymbol{x}$; and $F(t)$ is determined from (3.2) and (3.5). These equations represent a generalization of the axisymmetric thin-film equations (Yiantsios & Davis 1990, 1991).

The continuity equation (3.9) can be written as

$$\frac{\partial h}{\partial t} + \nabla_S\cdot(h\boldsymbol{u}) + (\boldsymbol{v}_{outer} - \boldsymbol{v}_0)\cdot\nabla_S\, h = 0. \tag{3.11}$$

If $\boldsymbol{v}_0 = \boldsymbol{v}_{outer}$, the last term in (3.11) drops out, and the system (3.6)–(3.11) obviously has an axisymmetrical solution, with h, p, $\boldsymbol{f}$, and $\boldsymbol{u}$ depending only on t and $r = (x_1^2 + x_2^2)^{1/2}$, given the axisymmetrical initial gap profile; otherwise, the film is necessarily non-axisymmetric (E. J. Hinch, personal communication). We have been unable to prove analytically that the fluid velocity from the outer solution at the point of contact, $\boldsymbol{v}_{outer}$, is the same as the velocity $\boldsymbol{v}_0$ of the geometrical contact point. However, it is possible to demonstrate this important fact numerically.

A representative example of two slightly non-touching spherical drops with $a_1/a_2 = 0.7$ was considered, the first sphere having an instantaneous unit velocity of its centre in the direction normal to the line of centres, while the centre of the second sphere is at rest. By calculating the fluid velocities v_1 and v_2 on the drop surfaces 1 and 2, respectively, at the axis of symmetry across the gap, a check has been made that both v_1 and v_2 approach the same value $v_0 = 1/(1 + 0.7) = 0.5882$, given by the lever rule, in the limit of touching. This Stokes problem is conveniently solved by multipole expansions, using Lamb's general solution and retaining a sufficient number of terms for each value of the gap (Zinchenko 1982). Results are shown in table 1 for two viscosity ratios, $\hat{\mu} = 1$ and $\hat{\mu} = 3$, and different values of the dimensionless surface

	$\hat{\mu}=1$		$\hat{\mu}=3$	
ϵ	v_1	v_2	v_1	v_2
0.1	0.656	0.396	0.7614	0.3475
0.03	0.620	0.526	0.6794	0.4825
0.01	0.607	0.573	0.6316	0.5460
0.003	0.600	0.589	0.6059	0.5758
0.001	0.596	0.593	0.5962	0.5855
0.0003	0.594	0.593	0.5920	0.5887
0.0001	0.592	0.592	0.5904	0.5893
0.00003	0.591	0.591	0.5896	0.5893

TABLE 1. Dimensionless fluid velocities on drop surfaces 1 and 2 as the gap goes to zero.

clearance $\epsilon = h_{min}/a_1$. Since $v_1 = v_2 = v_0$ in the limit $\epsilon \to 0$, we conclude that $\boldsymbol{v}_{outer} = \boldsymbol{v}_0$.

At the initial stage of approach, the deformation is necessarily axisymmetric, since it is a perturbation generated by the lubrication pressure between two spherical drops; the lubrication pressure is axisymmetrical because the normal relative motion provides the dominant contribution. So, the film will remain axisymmetric to leading order in the capillary number, so long as it is stable. Loss of stability, however, will most likely not occur until just prior to coalescence and so would not appreciably change the results of our calculations. The axial symmetry of the film, which is a crucial but not *ad hoc* simplification, allows rewriting of (3.6)–(3.11) in a cylindrical coordinate system moving with the gap in a form similar to (63)–(67) of Yiantsios & Davis (1990), the difference being in the inclusion of van der Waals pressure and the time-dependent driving force, $F(t)$. We introduce the non-dimensional variables $\tilde{t}$, $\tilde{h}$, $\tilde{p}$, $\tilde{f}$, and $\tilde{u}$ similar to Saboni, Gourdon & Chesters (1995):

$$h = \frac{b^2}{R}\,\tilde{h}, \quad r = b\tilde{r}, \quad p = \frac{\sigma}{2R}\,\tilde{p}, \quad f = \frac{b\sigma}{2R^2}\,\tilde{f}, \quad u = \frac{1}{2}\,\frac{b^2}{R^2}\,\frac{\sigma}{\mu'}\,\tilde{u}, \quad t = 2\,\frac{R^2}{b}\,\frac{\mu'}{\sigma}\,\tilde{t}, \tag{3.12}$$

where b is defined by the relation $\pi b^2\sigma/R = \Delta\rho g R^3$ and is a measure of the dimple radius, and $R = a_1a_2/(a_1 + a_2)$ is the reduced radius of the two drops. This non-dimensionalization, rather than that of Yiantsios & Davis (1990), is chosen in order to remove the artificial dependence on an arbitrary initial separation; the length scale b^2/R is then a characteristic value of the deformation length scale in the near-contact region.

With tildes over the non-dimensional variables henceforth omitted, the dimensionless equations take the form:

Normal stress balance

$$p - \frac{\delta}{h^3} = 2 - \frac{1}{r}\,\frac{\partial}{\partial r}\left(r\,\frac{\partial h}{\partial r}\right), \tag{3.13}$$

Momentum balance

$$f = -\frac{h}{2}\,\frac{\partial p}{\partial r}, \tag{3.14}$$

Local boundary integral

$$f(r) = 4\int_0^\infty \phi(r', r)\left[\frac{u}{r'^2} - \frac{1}{r'}\,\frac{\partial u}{\partial r'} - \frac{\partial^2 u}{\partial r'^2}\right]\,\mathrm{d}r', \tag{3.15}$$

Mass continuity

$$\frac{\partial h}{\partial t} + \frac{1}{r}\,\frac{\partial}{\partial r}\,(rhu) = 0, \tag{3.16}$$

Integral force balance

$$\int_0^\infty \left(p - \frac{\delta}{h^3}\right)\, r\mathrm{d}r = \alpha \cos\,\beta(t), \tag{3.17}$$

where, from (3.5)

$$\beta(t) = 2\arctan\,\left[\tan\,\left(\tfrac{1}{2}\beta_0\right)\exp(\zeta\, Ca^{1/2}\, t)\right], \tag{3.18}$$

$$\alpha = \frac{4}{3}\,\pi\,\frac{(k+1)^3}{k^2}\,\left(\frac{\Lambda_{12} - k^2\Lambda_{22}}{\Lambda_{22} + k\Lambda_{12}}\right), \quad \zeta = \frac{2}{3}\,\frac{\hat{\mu}}{(k+1)}\left[\frac{2\pi}{(1-k^2)}\,\frac{(\hat{\mu}+\frac{2}{3})}{(\hat{\mu}+1)}\right]^{1/2} T, \tag{3.19}$$

and $\phi(r', r)$ is the elliptic type Green's function:

$$\begin{aligned}\phi(r', r) &= \frac{1}{2\pi}\,\frac{r'}{(r^2 + r'^2)^{1/2}}\,\int_0^\pi \left[1 - \frac{2rr'\cos\theta}{r^2 + r'^2}\right]^{-1/2} \cos\theta\,\mathrm{d}\theta \\ &= \frac{1}{2\pi r}\,\left[-(r + r')E + \frac{(r^2 + r'^2)}{(r + r')}\,K\right],\end{aligned} \tag{3.20}$$

where E and K are the full elliptic integrals with modulus $2(rr')^{1/2}/(r + r')$. Finally, the non-dimensional Hamaker constant,

$$\delta = \frac{\pi^2}{3}\,\frac{A\sigma^2}{(\Delta\rho g)^3}\,\left(\frac{a_1 + a_2}{a_1 a_2}\right)^8, \tag{3.21}$$

represents the ratio of the molecular forces to lubrication forces when the characteristic length is the dimple radius. Only small values of δ are considered herein; the case $\delta = O(1)$ is less interesting because the effect of deformation on the coalescence efficiency turns out to be negligible in this case (see §6). Far from the gap region, the solution $h(t, r)$ should behave as (Yiantsios & Davis 1990, 1991)

$$h \sim \tfrac{1}{2}r^2 - \alpha\cos\beta\,\ln r + O(1), \tag{3.22}$$

where the first term represents, to leading order, the non-deformed shape.

Since the driving force $\alpha\cos\beta(t)$ is a slowly varying function of the non-dimensional time t, the method of two timings in analysing the system (3.13)–(3.17) might be appropriate (Cole 1968). However, we have found this idea difficult to implement, and so, in what follows, the capillary number Ca is simply taken as a small but finite parameter.

3.3. *Trajectory matching (general case)*

A proper transition should be made from the outer solution for the relative trajectory of two spherical drops without van der Waals attraction, approaching contact at $\beta = \beta_0$, to the inner solution of the thin-film equations; this time matching provides an initial condition $h(0, r)$ to integrate (3.13)–(3.17). According to the scaling (3.12), the deformation first becomes important at $t = O(1)$, when $h = O(1)$. At these times, the driving force, $\alpha\cos\,\beta(t)$, has nearly a constant value of $\alpha\cos(\beta_0)$, as follows from (3.18) and the constraint $Ca \ll 1$ (provided that β_0 is not close to $\pi/2$; the special case $\beta_0 \approx \pi/2$ is considered in §3.4). Additionally, the van der Waals disjoining pressure, $-\delta/h^3$, is still small for $h = O(1)$, compared to the other terms in (3.13) and (3.17) due to $\delta \ll 1$.

For the above reasons, the following matching procedure can be used. We start from some large non-dimensional minimum separation $h_0 \gg 1$ and non-deformed film shape $h = h_0 + r^2/2$ at $t = 0$, and integrate the system (3.13)–(3.17) with $\beta(t) = \beta_0$ and $\delta = 0$ until the moment $t = t_{coll}$, when two drops would collide if they stayed non-deformed without van der Waals attraction. This artificial collision time is given by

$$t_{coll} = \frac{3}{8}\,\frac{\sqrt{2}\,\pi^2}{\alpha}\,\frac{h_0^{1/2}}{\cos\beta_0}, \tag{3.23}$$

as follows from the near-contact asymptotics for two spherical drops (Davis *et al.* 1989; Zinchenko 1982; see Appendix A). Note that, while t_{coll} can be arbitrarily large with increasing h_0, the film profile $h(t_{coll}, r)$ becomes independent of h_0 when $h_0 \to \infty$ (because then, for most of the time in this integration, the deformation is unimportant). It is this profile which is the desired initial condition $h(0, r)$ for integration of (3.13)–(3.17) for the inner solution from $t = 0$ with a variable β-angle (3.18) and δ given by (3.21). We have found this initial $h(0, r)$ to be a slightly non-parabolic profile, practically insensitive to the initial separation h_0 for $h_0 > 10\alpha\cos\beta_0$. Thus, the matching condition in the present form does not contain arbitrary parameters and avoids pinpointing an exact position in time to switch from the spherical-drop outer solution to the thin-film inner solution for each trajectory.

3.4. *A special case:* $\beta_0 \approx \pi/2$; $(\pi/2 - \beta_0 = O(Ca^{1/3}))$

If the initial contact angle β_0 is close to $\pi/2$, then, as a detailed analysis shows (§6), the drops either coalesce or separate in the vicinity of $\beta = \pi/2$, and so the linearization of $\cos\beta(t)$ in (3.17) can be made for all t, using either (3.3) or (3.18). Introducing new non-dimensional variables $\hat{t}$, $\hat{r}$, $\hat{h}$, $\hat{p}$, $\hat{u}$, and $\hat{f}$ as

$$\hat{r} = \frac{r}{\omega^{1/3}\,Ca^{1/6}}, \quad \hat{h} = \frac{h}{\omega^{2/3}\,Ca^{1/3}}, \quad \hat{t} = \omega^{1/3}\,Ca^{1/6}t,$$
$$\hat{p} = p, \quad \hat{u} = \frac{u}{\omega^{2/3}\,Ca^{1/3}}, \quad \hat{f} = \frac{f}{\omega^{1/3}\,Ca^{1/6}}, \tag{3.24}$$

where $\omega = \alpha\zeta$, and α and ζ are defined by (3.19), the thin-film equations (3.13)–(3.17) with the linearized driving force take the form

$$\hat{p} - \frac{\hat{\delta}}{\hat{h}^3} = 2 - \frac{1}{\hat{r}}\,\frac{\partial}{\partial\hat{r}}\left(\hat{r}\,\frac{\partial\hat{h}}{\partial\hat{r}}\right), \tag{3.25}$$

$$\hat{f} = -\frac{\hat{h}}{2}\,\frac{\partial\hat{p}}{\partial\hat{r}}, \tag{3.26}$$

$$\hat{f} = 4\int_0^\infty \phi(\hat{r}', \hat{r})\,\left(\frac{\hat{u}}{\hat{r}'^2} - \frac{1}{\hat{r}'}\,\frac{\partial\hat{u}}{\partial\hat{r}'} - \frac{\partial^2\hat{u}}{\partial\hat{r}'^2}\right)\mathrm{d}\hat{r}', \tag{3.27}$$

$$\frac{\partial\hat{h}}{\partial\hat{t}} + \frac{1}{\hat{r}}\,\frac{\partial}{\partial\hat{r}}\,(\hat{r}\;\hat{h}\;\hat{u}) = 0, \tag{3.28}$$

$$\int_0^\infty \left(\hat{p} - \frac{\hat{\delta}}{\hat{h}^3}\right)\hat{r}\;\mathrm{d}\hat{r} = \hat{\xi}_0 - \hat{t}. \tag{3.29}$$

The new parameters, $\hat{\delta}$ and $\hat{\xi}_0 > 0$ are related to the old ones by

$$\hat{\delta} = \frac{\delta}{\omega^2 Ca}, \quad \beta_0 = \frac{\pi}{2} - \frac{Ca^{1/3}\omega^{2/3}\,\hat{\xi}_0}{\alpha}. \tag{3.30}$$

An advantage of the driving force linearization and the scaling (3.24) is that the size ratio, viscosity ratio, capillary number and dimensionless Hamaker constant have all been incorporated into one dimensionless parameter, $\hat{\delta}$, and results near $\pi/2$ can be easily transformed throughout the entire parameter space.

Matching with the outer trajectory is now handled simply by integrating (3.25)–(3.29) with the initial non-deformed shape $\hat{h} = \hat{h}_0 + \hat{r}^2/2$, where $\hat{h}_0 \gg 1$, from $\hat{t} = -\hat{t}_{coll}$, where $\hat{t}_{coll}$ is the time required for two drops to collide under the action of the driving force (3.2), linearized in time at $\beta \approx \pi/2$, if they stayed non-deformed without van der Waals attraction. This form of matching assumes that the outer trajectory would reach contact at $\hat{t} = 0$, as required. The expression for $\hat{t}_{coll}$ again can be obtained from the near-contact asymptotics for spherical drops (see Appendix A):

$$\hat{t}_{coll} = -\hat{\xi}_0 + \left[\hat{\xi}_0^2 + \tfrac{3}{4}\sqrt{2}\,\pi^2 \hat{h}_0^{1/2}\right]^{1/2}. \tag{3.31}$$

In the present paper, only small and moderate values of $\hat{\delta}$ are of interest. In this case, the system (3.25)–(3.29) should be integrated to $\hat{t} = O(1)$ or longer times, to determine whether the drops will touch (coalesce) or separate; the solution at these times is unaffected by the arbitrary initial separation $\hat{h}_0$, provided $\hat{h}_0 \gg 1$.

For $\pi/2 - \beta_0 = O(Ca^{1/3})$, which corresponds to $\hat{\xi}_0 = O(1)$, the axial symmetry of the film, to leading order in $Ca \ll 1$, is still a valid assumption. Indeed, when two spherical drops approach each other, the lubrication pressure from the normal relative motion is $O(F/(\epsilon a_i^2))$, where F is the driving force (3.2) and ϵa_1 is the minimum surface separation. The gap contribution from the transverse motion to the hydrodynamic forces should not exceed $O(F_i\epsilon)$, since the resistance coefficients T_{ij} are known to have finite derivatives with respect to ϵ at $\epsilon \to 0$ (Zinchenko 1980). From this and the $\cos\phi$-dependence of the pressure for the transverse motions on the azimuthal angle of rotation about the line of centres (Zinchenko 1980), we conclude that the normal stress in the gap region for the transverse motion is at most $O(F_i/(a_i^2\epsilon^{1/2}))$ and, hence, its ratio to the lubrication pressure for the normal motion is at most $O(\epsilon^{1/2}/\cos\beta)$. With $\cos\beta = O(Ca^{1/3})$, the lubrication pressure from the normal relative motion becomes comparable to the capillary pressure at $\epsilon = O(Ca^{4/3})$; the transverse motion contribution at these separations is at least $O(Ca^{-1/3})$ times smaller. Hence, the initial deformation is necessarily axisymmetric due to the dominant pressure from the normal motion, and, as before, there is no reason to expect the loss of axial symmetry of the film, as long as it remains stable.

3.5. *On the range of validity of the present theory*

A natural question is whether the assumption of small Reynolds numbers, $Re_i = V_i a_i \rho_e/\mu_e \ll 1$, is enough to neglect inertial effects in the gap region. Except for the very fast, quick stage of the film drainage, where the van der Waals attraction is dominant, an estimation of the role of inertia effects in the gap region for $\hat{\mu} = O(1)$ is made as follows. To leading order, the fluid velocity in the near-contact zone is finite, $O(V_i)$, and varies on the length scale $a_i\epsilon^{1/2}$ (where $\epsilon = O(h/a_i)$). The normal relative velocity is at most $O(V_i\epsilon^{1/2})$, which follows from the resistance law $\mathrm{d}h/\mathrm{d}t \sim V_i\epsilon^{1/2}$ (Davis *et al.* 1989) for non-deformed drops as the upper estimate. The parabolic

squeezing tangential fluid velocity (due to normal relative motion) is $O(\epsilon^{1/2}V_i)$ and varies on the length scale ϵa_i (Yiantsios & Davis 1990, 1991); the time scale for the velocity changes is at least $O(a_i\epsilon^{1/2}/V_i)$. It follows from these arguments that the neglected unsteady and convective terms ($\partial \boldsymbol{v}/\partial t$, $\boldsymbol{v}\cdot\nabla\,\boldsymbol{v}$) in the near-contact zone do not exceed $O(V_i^2/(a_i\epsilon^{1/2}))$. The viscous term $\mu\nabla^2\boldsymbol{v}$ is $O(\mu_e V_i/(a_i^2\epsilon^{3/2}))$ in the gap and $O(\mu' V_i/(a_i^2\epsilon))$ in the adjacent zones inside the drops. Comparison of the inertia and viscous terms thus shows that the condition $Re_i \ll 1$ for the Stokes approximation in the outer region is also sufficient to neglect inertia terms in the near-contact zone. For this reason, small inertial effects cannot act as a singular perturbation in the gap region (for solid spheres, this was shown by Cooley & O'Neill 1969 and by O'Neill & Stewartson 1967) and would give for $Re_i \ll 1$ only a small correction to the results of the present paper. In contrast, small deformation is a singular perturbation and can make the coalescence efficiency significantly different from that for spherical drops.

Besides $Re_i \ll 1$, another limitation of the present theory is the neglect of the next terms in the asymptotic thin-film equations (3.13)–(3.17). As follows from the analysis of Zinchenko (1978, 1982) for spherical drops with $\hat{\mu} \leqslant O(1)$, this neglect gives an $O(|\ln\epsilon|\epsilon^{1/2}/\hat{\mu})$ relative error in the resistance coefficient. Since deformation becomes important at $\epsilon \sim Ca$, we expect the asymptotic equations (3.13)–(3.17) to be valid for $|\ln Ca|Ca^{1/2}/\hat{\mu} \ll 1$. For $\hat{\mu} = O(1)$, the range $Ca^{1/2}|\ln Ca| \ll 1$ includes non-Brownian drops, considered in the present work. For example, two ≈ 50 μm drops with $a_1/a_2 \approx 0.7$ and density contrast $\Delta\rho \approx 0.1$ g cm^{-3} have $Ca \approx 10^{-5}$, but still extremely high Péclet number, $Pe \approx 10^6$; it was shown previously (Zinchenko & Davis 1994) that, even for much smaller $Pe \sim 10^4$, Brownian motion then has no appreciable effect on the collision efficiency.

Finally, for high viscosity ratio, $\hat{\mu} \gg 1$ (almost immobile interfaces), the validity of the thin-film equations used in the present work is limited to $\hat{\mu}Ca^{1/2} \ll 1$ (Yiantsios & Davis 1990, 1991). Besides, for $\hat{\mu} \to \infty$, the approximation of the film axial symmetry (which was shown to hold for $\hat{\mu} = O(1)$ and $Ca \ll 1$) may have a very narrow range of validity, but, unfortunately, we are unable to give appropriate estimates.

4. Numerical technique

To find the critical angle β_c, defined in §3, and study how the collision efficiency E_{12} depends on the parameters k, $\hat{\mu}$, Ca, and δ, the integro-differential system of equations (3.13)–(3.17) should be solved many thousand times, and it is essential to develop a very fast algorithm. Given the initial shape $h(0, r)$, a straightforward explicit approach would start from the normal stress balance (3.13) to calculate pressure p, then substitute p into the momentum balance (3.14) to find f, then use the inverted form of the boundary integral (3.15) to calculate the velocity u, and finally update the film shape from (3.16). Regardless of the technique to satisfy the integral balance (3.17), we have found that the explicit method or its modifications require an extremely small time step $\Delta t \leqslant \text{const}\times(\Delta r)^4$ for numerical stability, because the system (3.13)–(3.17) is very stiff. For example, for a typical value $\alpha\cos\beta \sim 5$ of the non-dimensional driving force in (3.17), a very tight stability constraint $\Delta t \leqslant 1.6\times10^{-5}$ was observed, even with a crude spatial resolution $(\Delta r)_{min} = 0.1$. Since the characteristic times $t \sim Ca^{-1/2}$ of tangential motion are of interest, we have found the explicit method to offer no prospect for obtaining accurate results and systematic applications to collision efficiency calculations (§6), especially in cases of very small Ca.

An alternative method, used by Yiantsios & Davis (1990, 1991) for the case of a constant driving force, is a nonlinear completely implicit finite-difference scheme

solved iteratively at each time step, so that, u, f, p, and h are found successively from (3.16), (3.15), (3.14), and (3.13) by integrations to form a new iterate. (Internal iterations are also necessary to satisfy the integral force balance (3.17) by adjusting $\partial h/\partial t$.) To guarantee convergence for relatively strong local deformations, a proper under-relaxation is necessary. Even with under-relaxation, the outer iterations tend to diverge when the time step Δt tends to zero, because of the inverse non-evolutional order of operations (3.16)–(3.13) in this method. Nevertheless, this approach is quite successful for drops with hydrodynamic interactions only. Difficulties occur when molecular forces are included; in this case, unfortunately, the relaxation parameter becomes prohibitively small, and the calculation stops long before coalescence occurs.

To overcome these difficulties, the following substantially new *matrix-iterative* method for solving the thin-film equations (3.13)–(3.17) was developed. First, a semi-implicit scheme is used to make (3.13)–(3.17) linear with respect to h, u, f, and p at a new time $t^{(v+1)}$, given the gap profile $h^{(v)}$ at the previous time $t^{(v)}$:

$$r\left\{p^{(v+1)} - \frac{\delta}{[h^{(v)}]^3}\right\} = -\frac{\partial}{\partial r}\left(r\,\frac{\partial H^{(v+1)}}{\partial r}\right), \tag{4.1}$$

$$\frac{2f^{(v+1)}}{h^{(v)}} = -\frac{\partial p^{(v+1)}}{\partial r}, \tag{4.2}$$

$$f^{(v+1)}(r) = 4\int_0^\infty \phi(r', r)\left[\frac{1}{r'^2} - \frac{1}{r'}\,\frac{\partial}{\partial r'} - \frac{\partial^2}{\partial r'^2}\right] u^{(v+1)}(r')\mathrm{d}r', \tag{4.3}$$

$$rq + \frac{\partial}{\partial r}\left[r\ h^{(v)}\ u^{(v+1)}\right] = 0, \tag{4.4}$$

$$\int_0^\infty \left[p^{(v+1)} - \frac{\delta}{[h^{(v)}]^3}\right] r\mathrm{d}r = \alpha\cos\beta(t), \tag{4.5}$$

where

$$H = h - \tfrac{1}{2}\,r^2, \quad q = \frac{h^{(v+1)} - h^{(v)}}{\Delta t} = \frac{H^{(v+1)} - H^{(v)}}{\Delta t}, \tag{4.6}$$

and a second-order finite-difference discretization with respect to r is used on a uniform mesh:

$$0 = r_0 < r_1 < r_2 < \ldots r_N = r_{max}. \tag{4.7}$$

The *matrix method*, in its most economical form, to solve (4.1)–(4.5) for $h^{(v+1)}$, $u^{(v+1)}$, $f^{(v+1)}$ and $p^{(v+1)}$, starts from (4.4) and gives the expression for $u^{(v+1)}(r_i)$ in terms of $q(r_j)\,(0 \leqslant j \leqslant i)$ by integrating from 0 to r_i using the trapezoidal rule. Substituting this expression into the finite-difference form of the boundary integral (4.3) leads to a matrix relation

$$\boldsymbol{f}^{(v+1)} = \boldsymbol{A}_1 \cdot \boldsymbol{q}, \tag{4.8}$$

with the bold letters denoting vectors of values at all mesh points $0, 1, \ldots, N$ and $\boldsymbol{A}_1$ being a $(N+1)\times(N+1)$ matrix. Equation (4.2) can be integrated next from r_{max} to r_i. Using the asymptotics of the exact solution at $r \to \infty$, where the deformation can be neglected,

$$f(r) = O(r^{-2}), \quad p(r) = O(r^{-3}) \tag{4.9}$$

(these relations are a simple consequence of (3.14)–(3.16) and (3.22)), the initial

condition for integrating (4.2) can be taken as

$$p_N^{(v+1)} = \frac{4}{3}\,\frac{f_N^{(v+1)}}{r_N}. \tag{4.10}$$

Thus, substituting (4.8) into (4.2) gives another matrix relation:

$$\boldsymbol{p}^{(v+1)} = \boldsymbol{A}_2 \cdot \boldsymbol{q}, \tag{4.11}$$

where $\boldsymbol{A}_2$ is a $(N+1)\times(N+1)$ matrix. Finally, substituting the pressure (4.11) into the normal stress balance (4.1) and integrating twice from 0 to r_i yields

$$\boldsymbol{H}^{(v+1)} = \boldsymbol{g} - \boldsymbol{T}\cdot\boldsymbol{q} + \boldsymbol{C}. \tag{4.12}$$

The vector $\boldsymbol{g}$ is a result of two-fold integration of (4.1), with the artificial condition $H_0^{(v+1)} = 0$ at the axis of symmetry and $p^{(v+1)}$ neglected. The contribution $-\boldsymbol{T}\cdot\boldsymbol{q}$ is solely due to $p^{(v+1)}$ in (4.1) (assuming, again, $H_0^{(v+1)} = 0$); $\boldsymbol{T}$ is another full $(N+1)\times(N+1)$ matrix; the vector $\boldsymbol{C} = (C, C, \ldots C)$, where the additive constant C (the film thickness at the axis of symmetry) has yet to be determined.

Taking into account (4.6) and (4.12) gives an equation for $\boldsymbol{q}$:

$$(\boldsymbol{T} + \Delta t\ \boldsymbol{I})\cdot\boldsymbol{q} = \boldsymbol{g} - \boldsymbol{H}^{(v)} + \boldsymbol{C}. \tag{4.13}$$

The vector $\boldsymbol{q}$ can be decomposed as

$$\boldsymbol{q} = \boldsymbol{q}^I + C\boldsymbol{q}^{II}, \tag{4.14}$$

where $\boldsymbol{q}^I$ and $\boldsymbol{q}^{II}$ are the solutions of (4.13) with the right-hand-side vectors being $\boldsymbol{g} - \boldsymbol{H}^{(v)}$ and $(1,\ldots,1)$, respectively. LU-factorization of the matrix $\boldsymbol{T} + \Delta t\ \boldsymbol{I}$ into a product of lower and upper triangular matrices is used to compute $\boldsymbol{q}^I$ and $\boldsymbol{q}^{II}$. The relations (4.11) and (4.14) imply $\boldsymbol{p}^{(v+1)} = \boldsymbol{p}^I + C\boldsymbol{p}^{II}$, where the pressures $\boldsymbol{p}^I = \boldsymbol{A}_2\cdot\boldsymbol{q}^I$ and $\boldsymbol{p}^{II} = \boldsymbol{A}_2\cdot\boldsymbol{q}^{II}$ are independent of C. Finally, substituting $\boldsymbol{p}^{(v+1)} = \boldsymbol{p}^I + C\boldsymbol{p}^{II}$ into the integral force balance (4.5) gives the equation for the scalar C; the tail of the integral (4.5) (over $r \geqslant r_{max}$) is approximated as $p_N^{(v+1)} r_N^2$, using the asymptotics (4.9); the van der Waals pressure contribution to the tail is neglected. Knowing q yields $h^{(v+1)}$ and allows us to proceed to the next time step.

Most importantly, this non-iterative algorithm is *absolutely stable,* as was observed in all numerical experiments, so that the time step is only limited by accuracy requirements. However, the cost of LU-factorization of the matrix $(\boldsymbol{T} + \Delta t\ \boldsymbol{I})$ is $O(N^3)$ (the other parts of the algorithm, in the optimal form, are $O(N^2)$–intensive and much faster). To considerably speed up the method, these LU-factorizations are made only at rare selected instants of time (see below). At intermediate steps, (4.13) for $\boldsymbol{q}^I$ and $\boldsymbol{q}^{II}$ is solved iteratively, using the last-obtained factorization $\boldsymbol{L}\cdot\boldsymbol{U}$ to precondition (Hageman & Young 1981) the system (4.13). Namely, the factorization $\tilde{\boldsymbol{L}}\cdot\tilde{\boldsymbol{U}}$ of the matrix $(\boldsymbol{T} + \Delta t\ \boldsymbol{I})$ at some close preceding time, $t = t^{(k)}$, can be considered as an approximate factorization of $\boldsymbol{T} + \Delta t\,\boldsymbol{I}$ at $t = t^{(v)}$, and so multiplying (4.13) by $(\tilde{\boldsymbol{L}}\cdot\tilde{\boldsymbol{U}})^{-1}$ makes the system matrix close to the identity matrix, which allows very fast simple iterations (ℓ being the number of the iteration):

$$\boldsymbol{q}_{(\ell+1)} = \boldsymbol{q}_{(\ell)} - \tilde{\boldsymbol{U}}^{-1}\cdot\tilde{\boldsymbol{L}}^{-1}\cdot\boldsymbol{R}_{(\ell)} \tag{4.15}$$

where

$$\boldsymbol{R}_{(\ell)} = (\boldsymbol{T} + \Delta t\ \boldsymbol{I})\cdot\boldsymbol{q}_{(\ell)} - (\boldsymbol{g} - \boldsymbol{H}^{(v)}) - \boldsymbol{C}. \tag{4.16}$$

The iterative process (4.15) is performed twice: the first time with $C = 0$, and the second time setting $\boldsymbol{g} - \boldsymbol{H}^{(v)} = 0$ and $C = 1$, to generate $\boldsymbol{q}^I$ and $\boldsymbol{q}^{II}$ separately (an

alternative way of iterating the combination $\boldsymbol{q}^I + C\boldsymbol{q}^{II}$ was unsuccessful); in both cases, a linear extrapolation of $\boldsymbol{q}^I$ or $\boldsymbol{q}^{II}$ from two preceding steps serves as a good initial approximation. Obviously, the calculation of the residual $\boldsymbol{R}_{(\ell)}$ does not require any matrix operations, but only substituting $\boldsymbol{q}^I$ or $\boldsymbol{q}^{II}$ into (4.4), with successive integrations (4.4)–(4.1) (which makes this part of the algorithm closer to the code of Yiantsios & Davis 1990, 1991, although the iterative scheme (4.15) is quite different). When iterating $\boldsymbol{q}^I$, the residual $\boldsymbol{R}_{(\ell)}$ can be found as $\boldsymbol{H}^{(v)} - \boldsymbol{H}^{(v+1)} + \boldsymbol{q}^I_{(\ell)}\Delta t$, where $\boldsymbol{H}^{(v+1)}$ is the result of the integration of (4.1) with $H_0^{(v+1)} = 0$. When iterating $\boldsymbol{q}^{II}$, the residual $\boldsymbol{R}_{(\ell)}$ takes the form $\boldsymbol{q}^{II}\Delta t - \boldsymbol{H}^{(v+1)}$, where $\boldsymbol{H}^{(v+1)}$ is the result of the integration of (4.1) with $\delta = 0$ and the axial thickness $H_0^{(v+1)} = 1$.

The cost of each iteration (4.15) is $O(N^2)$ and comes mostly from the boundary-integral evaluation (4.3) and matrix multiplications in (4.15). The frequency of factorizations (typically, every 15–25 time steps, when $N = 100-200$) is chosen so that the factorization costs would be small (20%) compared to the total cost of iterative solutions between factorizations. For intermediate steps, between factorizations, typically 3–4 iterations suffice in (4.15). Thus, this economical absolutely stable algorithm is, on average, $O(N^2)$-intensive per time step. The idea of this algorithm was prompted by the success of a similar procedure with preconditioning in a recent algorithm for random close packing (Zinchenko 1994).

To keep the $O(N^{-2})$ accuracy of spatial discretization, the boundary integral (3.15) is written as

$$\int_0^{r_{max}} \psi(r', r) \left[K - \ln \frac{r + r'}{|r - r'|} - \frac{(r + r')^2}{r^2 + r'^2} E \right] \mathrm{d}r' + \int_0^{r_{max}} \psi(r', r) \ln \frac{r + r'}{|r - r'|} \mathrm{d}r', \quad (4.17)$$

with

$$\psi(r', r) = \frac{1}{2\pi} \frac{(r^2 + r'^2)}{r(r + r')} \left[\frac{1}{r'^2} - \frac{1}{r'} \frac{\partial}{\partial r'} - \frac{\partial^2}{\partial r'^2} \right] u(r'). \quad (4.18)$$

The first regular integral (4.17) is approximated by the trapezoidal rule; for the second one, the weight ψ is linearly interpolated in each interval (r'_j, r'_{j+1}), and the corresponding integrals over (r'_j, r'_{j+1}) are taken analytically (the more standard procedure of subtracting the logarithmic singularity gives a larger, $O(N^{-2} \ln N)$ error).

Another feature of our algorithm for integrating (3.13)–(3.17) is an adaptive time step, $\Delta t = c_{\Delta t} h_{min}^{1/2}/\alpha$, where h_{min} is the minimum film thickness and the coefficient $c_{\Delta t} \ll 1$ is independent of α. Similarly, to keep high spatial resolution only in the significant region, a variable value $r_{max} = c_R h_{min}^{1/2}$ of the cut-off radius is set before each new factorization, with $c_R = \text{const} \gg 1$. For drops approaching each other, this leads to mesh contraction, and the new values of H are obtained by interpolation. For separating surfaces, when h_{min} increases, the asymptotic form (3.22), with the constant $O(1)$ estimated at the old value of r_{max}, is additionally used to expand the mesh. Both strategies for adapting Δt and r_{max} are applied only when there is no dimple. At the stage of the film drainage with a dimple present, both Δt and r_{max} are kept constant; in the latter case, the cut-off radius r_{max} turns out to be much larger than the dimple radius for the values of $c_R = 10$–20 used.

Finally, an important feature of the algorithm is to double the number of spatial nodes at the stage of the film drainage when van der Waals attraction is important (i.e. when the van der Waals pressure $-\delta/h^3$ contributes at least 20% to the total integral force balance (3.17)).

With $\beta(t) \equiv 0$, equations (3.13)–(3.17) describe the film drainage under the action

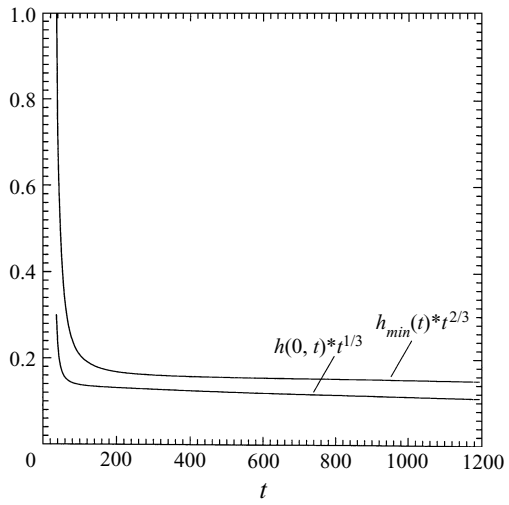

FIGURE 3. The long-time asymptotic behaviour of the film thickness $h(0,t)$ at the axis of symmetry and minimum thickness $h_{min}(t)$, for constant driving force ($\beta \equiv 0$, $\alpha = 1$) and no van der Waals attraction.

of a constant driving force. In this case, it is possible to make comparisons with existing solutions to check our code. The long-time asymptotic forms (69) and (70) of Yiantsios & Davis (1990) for the film drainage without van der Waals attraction, re-written in our new non-dimensional variables, take the form

$$h(0,t) \sim 0.14\alpha^{5/6}t^{-1/3}, \quad t \to \infty, \tag{4.19}$$

$$h_{min}(t) \sim 0.14\alpha^{2/3}t^{-2/3}, \quad t \to \infty. \tag{4.20}$$

To verify (4.19)–(4.20), the system (3.13)–(3.17) with $\delta = 0$, $\beta(t) \equiv 0$, $\alpha = 1$ (the relations (3.18)–(3.19) become irrelevant in this case) was solved numerically by our new algorithm, starting from the non-deformed shape $h(r,0) = h_0^{(0)} + r^2/2$ with the initial minimum thickness $h_0^{(0)} = 30$. Using $N = 100$–200, $c_R = 10$–20 and different time steps, the numerical convergence was achieved to within 1%, both for the axial $h(0,t)$ and the minimum $h_{min}(t)$ thicknesses in the wide time range $t \leqslant 1200$. The results shown in figure 3 indeed demonstrate that the quantities $h(0,t)\,t^{1/3}$ and $h_{min}(t)\,t^{2/3}$ approach constant values at $t \to \infty$ of about 0.11 and 0.15, respectively, in reasonably good agreement with (4.19)–(4.20) obtained by Yiantsios & Davis (1990) as a visual best fit in a more limited time range.

Saboni *et al.* (1995) have recently presented several calculations of the film drainage under the action of a constant force, with and without van der Waals attraction. In the case $\beta(t) \equiv 0$, and $\alpha = 1$, equations (3.13)–(3.17) are equivalent to those of Saboni *et al.* (1995), if our non-dimensional variables t, r, h, and δ are related to their t^*, r^*, h^*, and A^* as follows:

$$t^* = t/2, \quad r^* = r, \quad h^* = 2h, \quad A^* = 12\delta. \tag{4.21}$$

Unfortunately, for the same initial condition $h^* = 4 + (r^*)^2$ and the same values of A^*, several noticeable discrepancies were detected between our calculations and those of Saboni *et al.* (1995). For $A^* = 0$, their figure 2 gives the long-time asymptotic value of the dimple radius (where $h = h_{min}$) as $r_D^* \approx 1.25$, which is in disagreement with the simple Derjaguin and Kussakov formula $r_D^* = 1$ (see, e.g. Yiantsios & Davis

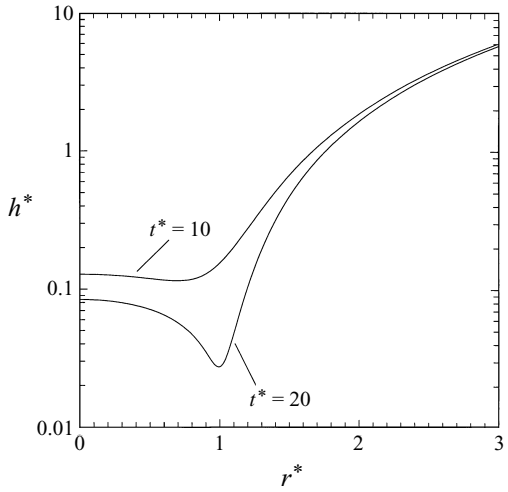

FIGURE 4. Non-dimensional film profile $h^*(r^*)$ at different times, for constant driving force with van der Waals attraction ($A^* = 10^{-4}$). The calculations using different program parameters $N = 100$–200, $c_R = 10$–20, and $c_{\Delta t} = 0.003$–0.007 give graphically indistinguishable results and locate the dimple radius to about 1% accuracy.

1990). For comparison, our numerical solutions yield $r_D^* = 0.99$–1.00 for all $t^* \geqslant 35$. When $A^* = 10^{-4}$, our accurate calculations give $r_D^* \approx 0.70$ and $r_D^* \approx 0.99$ for $t^* = 10$ and 20, respectively (figure 4), instead of $r_D^* \approx 1.15$ and $r_D^* \approx 1.22$, respectively, from figure 8 of Saboni *et al.* (1995) at the same times, respectively. In this case, the further film drainage results in a quick coalescence at $t^* = t_c^* \approx 21.1$, as shown in figure 5, where different time steps, different values of the cut-off radius, and different $N \leqslant 400$ (i.e. up to 800 spatial nodes at the last stage of approach) were used to demonstrate excellent numerical convergence. In contrast, according to figure 8 of Saboni *et al.* (1995), $t^* = 25$ is still prior to coalescence (paradoxically, their figures 9 and 10 suggest a different value of t_c^*, between 20 and 25). For relatively strong van der Waals attraction, $A^* = 10^{-2}$ and 10^{-3}, when the coalescence time is weakly sensitive to the details of the solution, the values of t_c^* from our figure 5 are in very good agreement with those from figure 9 of Saboni *et al.* (1995). However, for weak van der Waals attraction, $A^* = 10^{-5}$, our convergent value of $t_c^* \approx 37.8$ (figure 5) is, again, noticeably different from their $t_c^* \approx 44$.

We believe there may be two main reasons for these discrepancies. First, unlike in our (4.4), Saboni *et al.* (1995) use the continuity equation (3.16) as a linear implicit equation for $h^{(v+1)}$, but otherwise their method remains explicit, because the thickness $h^{(v+1)}$ found from (3.16) is then used to calculate pressure from (3.13), followed by the calculation of f from (3.14) and u from (3.15). Our experience shows that this modification of the explicit method does not alleviate the problem of the numerical stiffness, and, for fine spatial resolutions, the time steps would still have to be extremely small (unfortunately, the number of nodes and the spatial and time steps used are unavailable from Saboni *et al.* (1995) to check this conclusion). Second, the leading asymptotic $u = O(r^{-1})$ at $r \to \infty$ does not contribute to the integrand of (3.15), and so the term in the brackets of (3.15) is expected to behave like $O(r'^{-4})$ at $r' \to \infty$, while $f(r)$ decays only like $O(r^{-2})$ at $r \to \infty$. For this reason, the inverted form of the boundary integral (3.15) used by Saboni *et al.* (1995) is a much more slowly convergent integral at infinity than the direct form (3.15). This may also be a source

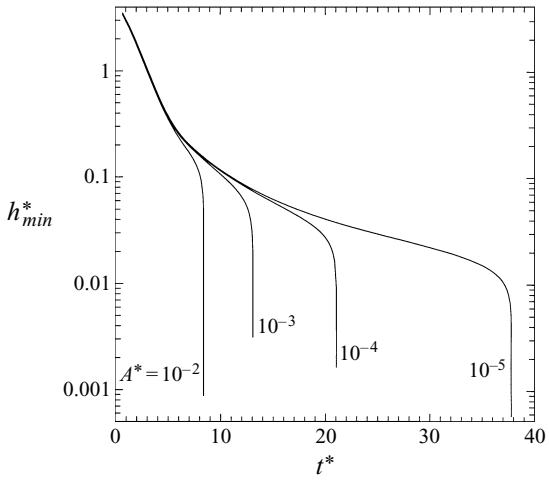

FIGURE 5. Time evolution of the minimum film thickness $h^*_{min}(t^*)$ for a constant driving force and different values of the non-dimensional Hamaker constant A^*. For each A^*, the four calculations using (i) $N = 200$, $c_{\Delta t} = 0.02$, $c_R = 10$, (ii) $N = 200$, $c_{\Delta t} = 0.01$, $c_R = 10$, (iii) $N = 400$, $c_{\Delta t} = 0.02$, $c_R = 10$, and (iv) $N = 400$, $c_{\Delta t} = 0.02$, $c_R = 20$ give graphically indistinguishable results and at least 0.5% accuracy in the coalescence times.

of inaccuracies. The difficulties of the explicit method for solving thin-film equations have been recognized (Davis *et al.* 1986; Yiantsios & Davis 1990, 1991), and it remains unclear, in view of the observed discrepancies, whether the modification of the explicit method by Saboni *et al.* (1995) can be a successful alternative to the more complicated technique of the present paper.

5. Comparison with full boundary-integral calculations

As for any asymptotic approach, the range of validity of our method described in §3 can be determined only by exact calculations which do not assume small deformations. To this end, it has proved particularly valuable to make a comparison with a full three-dimensional boundary-integral solution for two drops settling under gravity without van der Waals attraction for a small but finite capillary number when numerical convergence can still be reached. We have recently developed a novel version of a three-dimensional boundary-integral code, which has, in particular, relatively soft stability constraints and allows therefore very high surface resolutions (Zinchenko, Rother & Davis 1997). Using this algorithm, the gravity-induced motion of two drops with $\hat{\mu} = 1$, $a_1/a_2 = 0.7$, and $Ca = 0.145$ was calculated (figure 6); initially, the drops were non-deformed spheres with the horizontal and vertical centre-to-centre offsets $0.325a_2$ and $5.09a_2$, respectively (not shown). In this case, spherical drops would collide at $\beta = \beta_0 = 29.3^\circ$; in contrast, deformable drops come into 'apparent contact,' but do not touch (see below), and eventually separate (figure 6).

Figure 7 demonstrates that the main assumption of the asymptotic approach of §3, namely that the tangential relative motion in apparent contact is unaffected by small deformations to leading order in $Ca \ll 1$, is very accurate for Ca as large as 0.145. For non-deformed drops, $\ln\tan(\beta/2)$ would be a linear function of $\kappa T t$ with unit slope, as follows from (3.5). For comparison, $\ln\tan(\beta/2)$ vs. $\kappa T t$ from the boundary-integral solution is presented in figure 7, using the value of $T = 0.2913$ for two touching

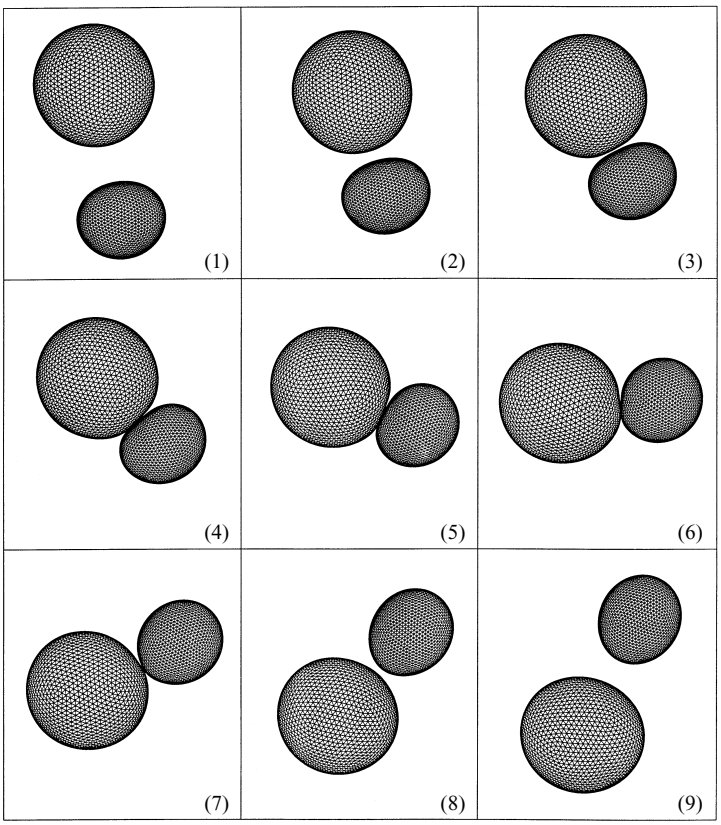

FIGURE 6. Gravity-induced relative motion of two drops with $a_1/a_2 = 0.7$, $\hat{\mu} = 1$, and $Ca = 0.145$ by a full boundary-integral algorithm (Zinchenko *et al.* 1997) using $N_\Delta = 3840$ triangular elements per drop. Drop relative positions (1)–(9) are shown at increasing times with a fixed increment.

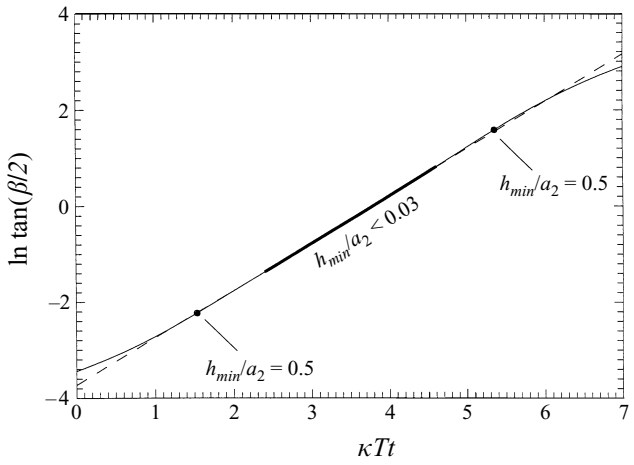

FIGURE 7. Tangential motion of drops in apparent contact for the simulation shown in figure 6; β is the angle between the line connecting the surface centroids and the vertical; t is the dimensional time; k and T are defined in (3.4). The solid line is from the boundary-integral simulation, and the dashed line (slope 0.984) is the best linear fit in the range of dimensional surface separations $h_{min} < 0.03a_2$.

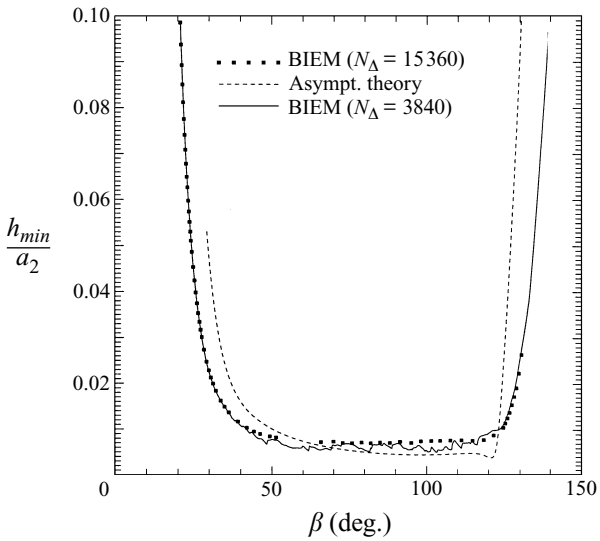

FIGURE 8. Comparison between the full boundary-integral simulation shown in figure 6 and the asymptotic theory. For the motion in apparent contact, the surface-to-surface minimum separation h_{min}, scaled with the larger radius a_2, is shown vs. β-angle. The boundary-integral calculations are for both 3840 and 15 360 triangular elements per drop, showing good convergence.

spherical drops with $k = 0.7$ and $\hat{\mu} = 1$; this dependence is almost linear, and the slope 0.984 of the best linear fit in the range of small separations $h_{min}/a_2 < 0.03$ is, indeed, very close to unity.

We could not quantify the second main simplification of the asymptotic theory of §3, namely to check how close the film shape is to axisymmetric; one of the difficulties is that $Ca = 0.145$ is not small enough, and some small but noticeable global deformation (figure 6) does not allow us to choose the reference axis properly. Instead, we have simply compared the minimum separation h_{min} vs. β for the boundary integral and asymptotic calculations. In the boundary-integral solution, h_{min} is rigorously calculated as the clearance between two surfaces with flat triangulation (see Zinchenko *et al.* 1996 for details). To check the convergence, the boundary-integral simulation was repeated with 15 360 triangles per drop (which took, however, several weeks of background calculations on an IBM AIX RISC/6000 workstation). The agreement between the results for $N_\Delta = 3840$ and 15 360 is very good (figure 8), considering how delicate the surface clearance is, about $0.007a_2$, for the motion in 'apparent contact.'

The much easier asymptotic calculation (dashed line in figure 8) was implemented using the matching procedure of §3.3 and the numerical technique of §4. The asymptotic solution is surprisingly accurate both in describing $h_{min}(\beta)$ and the 'separation angle' $\beta \approx 120^\circ$; much better agreement could not have been expected, because the relative size of the inner region, $O(Ca^{1/2})$, is not very small for this case (in contrast, the effect of deformations on the tangential motion is likely to be $O(Ca)$). The success of the comparison in figure 8 suggests that our asymptotic approach is quite accurate for smaller $Ca \leqslant 0.01$ ($\hat{\mu} = 1$ was chosen only to simplify the boundary-integral calculations, and the same conclusion is expected for any $\hat{\mu} = O(1)$). On the other hand, it would be very problematic to perform convergent full three-dimensional boundary-integral calculations for $Ca \leqslant 0.01$, even on the fastest supercomputers, because of (i) very tight stability constraints in this case, (ii) localization of stress

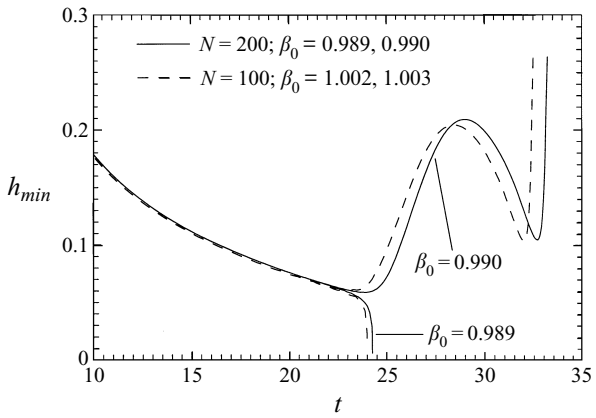

FIGURE 9. Time evolution of the minimum gap thickness for two trajectories near the critical β_0-angle for $k = 0.5$, $\hat{\mu} = 1$, $Ca = 2.2 \times 10^{-3}$, and $\delta = 1.1 \times 10^{-3}$.

in a very small near-gap region, and (iii) extremely small surface separations which two slightly deformable drops can reach. Thus, the asymptotic approach and the boundary-integral method substantially complement one another.

6. Results

Application of the above theory and numerical methods allows systematic study of the collision efficiency of sedimenting drops as a function of size ratio, k, viscosity ratio, $\hat{\mu}$, dimensionless Hamaker constant, δ, and capillary number, Ca. As an example of our trial-and-error procedure, figure 9 displays the evolution of the thin gap for β_0-angles near the critical value required to determine the collision efficiency. For $N = 100$ (and, accordingly, 200 spatial nodes at the stage of significant van der Waals attraction), the critical β_0-value, β_c, lies between 1.002 and 1.003 radians when $k = 0.5$, $\hat{\mu} = 1$, $\delta = 1.1 \times 10^{-3}$ and $Ca = 2.2 \times 10^{-3}$. As a convergence check, using $N = 200$ resulted in a change in β_c of 1.3% relative error ($0.989 < \beta_c < 0.990$). Much smaller time steps and much larger cut-off radii have similar small effects on the bounds for β_c, about 1%, acting in opposite directions. For $N = 100$, $c_{\Delta t} = 0.02$ and $c_R = 10$, which are typical for the calculations below, the two trajectories for $\beta = 1.002$ and 1.003 in figure 9 take 3.5 and 6 minutes, respectively, on an IBM AIX RISC/6000 workstation. A value of $c_{\Delta t} = 0.01$ was also often used in the calculations.

For trajectories with greater-than-critical horizontal offset, the minimum separation between the drops is a complex function of time. As figure 9 shows, for $\beta_0 = 0.990$ there are a local maximum and a local minimum in h_{min} after closest approach before the drops finally separate. The corresponding gap profiles at various instants in time are given in figure 10 for the same parameter values as in figure 9 with $N = 200$ and $\beta_0 = 0.990$. Comparison of the two figures reveals that, by the initial time in figure 10 ($t = 8.66$), a dimple has already formed for $\beta_0 = 0.990$. The radius of the dimple decreases with decreasing minimum separation until $t \sim 23.91$ with $\beta \sim 1.50$ radians, where h_{min} takes its smallest value. The dimple radius continues to decrease as β passes through $\pi/2$, but now the minimum separation increases until $\beta \sim 1.61$ radians at $t \sim 29.01$. Subsequently, h_{min} decreases until the dimple disappears at $t \sim 32.64$ and $\beta \sim 1.70$. Thereafter, separation of the two drops is very rapid.

Spherical drops both with and without van der Waals attraction have a single

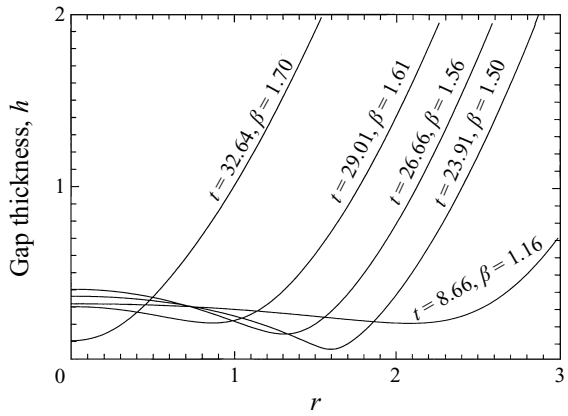

FIGURE 10. Dynamics of the thin-film gap profile for a trajectory close to critical, with $k = 0.5$, $\hat{\mu} = 1$, $Ca = 2.2 \times 10^{-3}$, and $\delta = 1.1 \times 10^{-3}$.

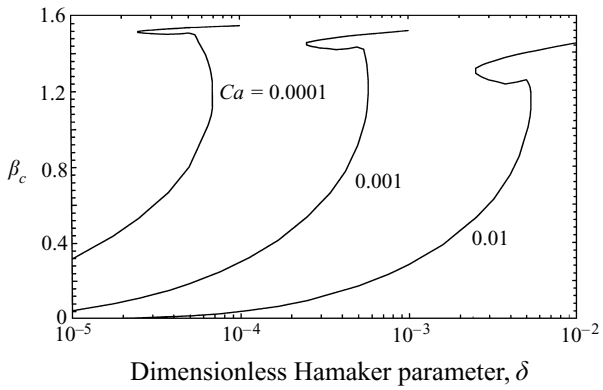

FIGURE 11. Critical β_0-angle as a function of the dimensionless Hamaker parameter for $k = 0.5$, $\hat{\mu} = 1$, and various Ca. The existence of a second coalescence region is indicated near $\beta_c = \pi/2$ by an open loop in each curve.

coalescence zone, such that a horizontal offset exceeding a critical value always leads to separation of the two drops, while smaller horizontal offsets always result in coalescence. The case of slightly deformable drops in the presence of molecular forces displays a more complex behaviour. The complicated interplay of deformation and van der Waals forces produces a second coalescence zone for certain dimensionless parameter values where β_c is close to $\pi/2$. Figure 11 is a graph of the critical β_0-angle vs. the dimensionless Hamaker parameter at capillary numbers of 0.0001, 0.001 and 0.01. It should be noted that these results, indicating a second coalescence zone for slightly deformable drops, have been confirmed both by calculations from (3.13)–(3.17) and by using (3.25)–(3.29) from the linear expansion of $\cos\beta$ near $\pi/2$. From figure 11, for example, two coalescence regions exist for $k = 0.5$, $\hat{\mu} = 1$, $Ca = 0.001$, and $\delta = 0.00055$. When the initial β-angle is between 0 and 1.019 radians, two sedimenting drops will always coalesce. For β_0 between 1.019 and 1.392 radians, the drops will pass by one another. However, when β_0 is between 1.392 and 1.495 radians, the drops once again collide, while initial angles greater than 1.495 radians lead to drop separation.

Figures 12 and 13 help to explain the second coalescence zone. Figure 12(*a*)

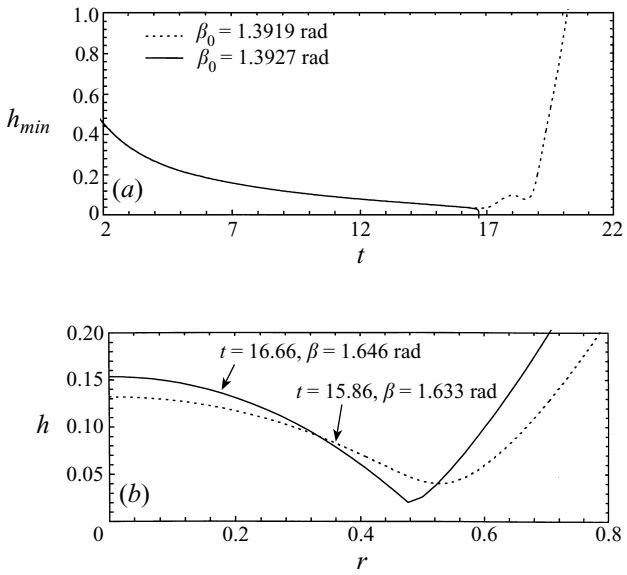

FIGURE 12. (*a*) Evolution of the thin gap and (*b*) dynamics of the gap profile, indicating rim rupture, near the onset of the second coalescence region ($\beta_c \sim 1.392$), for $k = 0.5$, $\hat{\mu} = 1$, $Ca = 0.001$, and $\delta = 0.00055$.

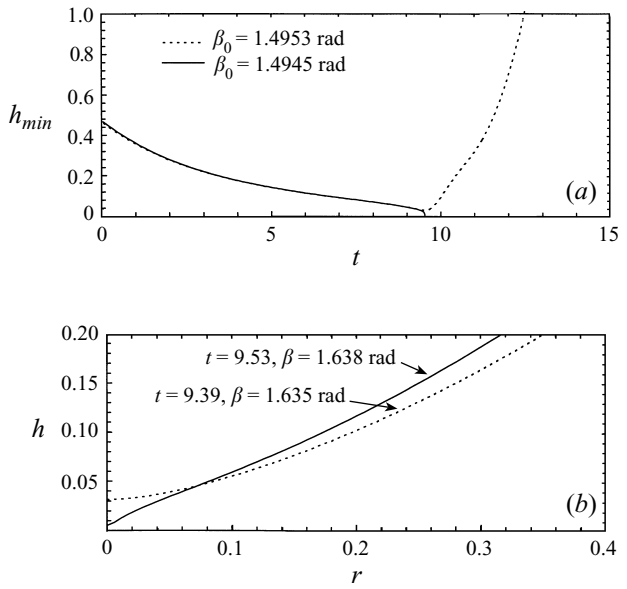

FIGURE 13. (*a*) Evolution of the thin gap and (*b*) dynamics of the gap profile, indicating nose rupture, near the upper limit of the second coalescence region ($\beta_c \sim 1.495$), for $k = 0.5$, $\hat{\mu} = 1$, $Ca = 0.001$, and $\delta = 0.00055$.

shows two near-limiting trajectories near $\beta_0 = 1.392$ radians displayed as h_{min} vs. t, while figure 12(*b*) gives two dimensionless gap profiles just before coalescence with $\beta_0 = 1.3927$ radians. The mode of coalescence indicated here is rim rupture, wherein the drops make contact at the edge of the dimple radius. Figure 13 is analogous to figure 12, except that the region considered is near $\beta_0 = 1.495$ radians. There

is no indication of a local maximum or minimum in h_{min} vs. t as in figure 12(a), because no dimple forms. Moreover, figure 13(b) indicates nose rupture as the mode of coalescence. In this case, the drops touch along the axis of symmetry as van der Waals forces pull them together.

The existence of a second coalescence zone is connected to the transition between rim rupture and nose rupture of the drops. When the gravitational driving force along the line of centres is sufficiently weak (β_0 is close to $\pi/2$), there is a range of dimensionless Hamaker parameters for which both modes of rupture can occur. In the first coalescence zone, where β_0 is not close to $\pi/2$, the drops touch before β reaches $\pi/2$. Van der Waals forces are weak enough to allow the pressure to build up in the region of near contact and cause a dimple to form before inducing collision. Thus, the mode of rupture is always rim rupture. Moreover, in this region, the dimple radius has just begun to decrease at the time of coalescence. In the second coalescence zone, where β_0 is close to $\pi/2$, the lower β_c value is due to another occurrence of rim rupture, and the upper β_c value is due to nose rupture. In both cases, coalescence occurs after β has passed through $\pi/2$, and thus the net driving force is negative (see (3.17)). In this region, the nose rupture may occur after a dimple has formed and disappeared.

Once the critical β_0-angles are known, the collision efficiency can be calculated. From Zhang & Davis (1991), for spherical drops without molecular forces, the trajectory equation can be integrated to yield

$$\frac{y_0}{s\sin\beta} = \exp\left(-\int_s^\infty \frac{M-L}{sL}\,\mathrm{d}s\right), \tag{6.1}$$

where $y_0 = 2d_\infty/(a_1+a_2)$ is the dimensionless horizontal offset, s is the centre-to-centre distance between drops, also made dimensionless by the average drop radius, and L and M are relative mobility functions for spherical drops along and normal to the line of centres, respectively (Haber *et al.* 1973; Zinchenko 1980). For spherical drops without van der Waals attraction, the limiting trajectory has $\beta = \pi/2$ at $s = 2$, so that from (6.1) the collision efficiency for spherical drops without van der Waal attraction, E_0, becomes

$$E_0 = \tfrac{1}{4}\,y_c^2 = \left[\frac{d_\infty^*}{a_1+a_2}\right]^2 = \exp\left(-2\int_2^\infty \frac{M-L}{sL}\,\mathrm{d}s\right), \tag{6.2}$$

where y_c is the dimensionless critical offset parameter. The calculation of collision efficiencies of spherical drops in the presence of van der Waals attraction is described in Appendix B.

On the limiting trajectory, slightly deformable drops come into apparent contact ($s \approx 2$) at $\beta = \beta_c$. Thus, also from (6.1) for the case of one critical β_0-angle, the collision efficiency for slightly deformable drops in the presence of van der Waals attraction, E_{12}, is given by

$$E_{12} = \sin^2\beta_c \exp\left(-2\int_2^\infty \frac{M-L}{sL}\,\mathrm{d}s\right). \tag{6.3}$$

By comparing (6.3) and (6.2) it is seen that

$$\frac{E_{12}}{E_0} = \sin^2\beta_c. \tag{6.4}$$

When there are two coalescence zones, with three critical β_0-angles, such that $\beta_{c,1} <$

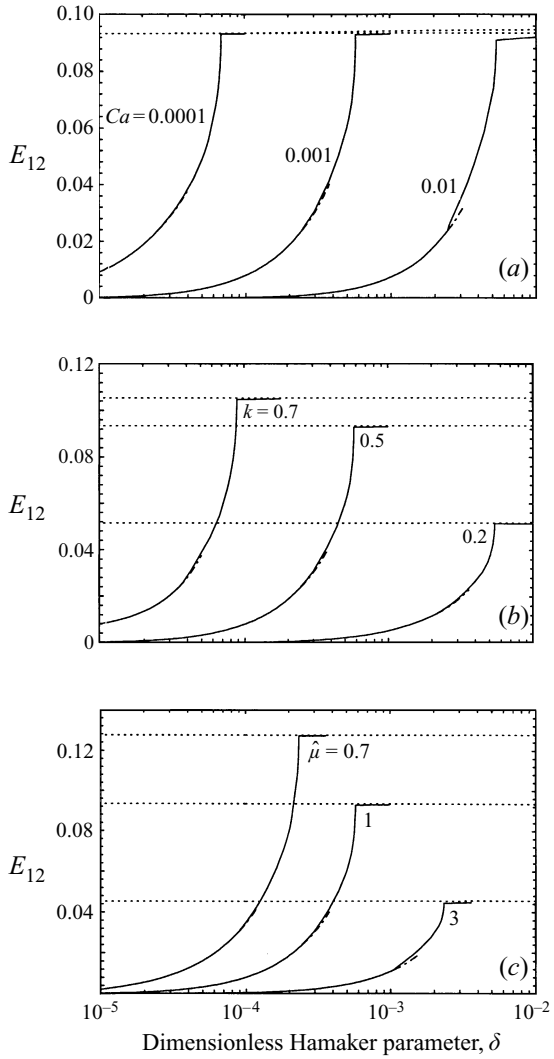

FIGURE 14. The collision efficiency for gravitational sedimentation of drops as a function of the dimensionless Hamaker parameter with (*a*) $k = 0.5$, $\hat{\mu} = 1$ at $Ca = 0.0001$, 0.001 and 0.01; (*b*) $Ca = 0.001$, $\hat{\mu} = 1$ at $k = 0.2$, 0.5, and 0.7, and (*c*) $k = 0.5$, $Ca = 0.001$ at $\hat{\mu} = 0.5$, 1, and 3. The dashed lines are for spherical drops in the presence of van der Waals forces; the solid lines are for slightly deformable drops in the presence of van der Waals forces; and the dash-dotted lines mark a discontinuity in the first derivative, neglecting the presence of the second coalescence region.

$\beta_{c,2} < \beta_{c,3}$, the collision efficiency is given by generalization of (6.4) as

$$E_{12} = E_0 (\sin^2 \beta_{c,3} - \sin^2 \beta_{c,2} + \sin^2 \beta_{c,1}). \tag{6.5}$$

It is noted that, owing to the form of (6.5), there are two discontinuities in the first derivative of the collision efficiency as a function of any one of the four governing dimensionless parameters with the other three fixed.

Figures 14 and 15 provide general trends for the collision efficiency as a function of various combinations of the four dimensionless parameters, k, $\hat{\mu}$, δ and Ca. In figure 14, the dimensionless Hamaker constant is the independent variable, and each of the

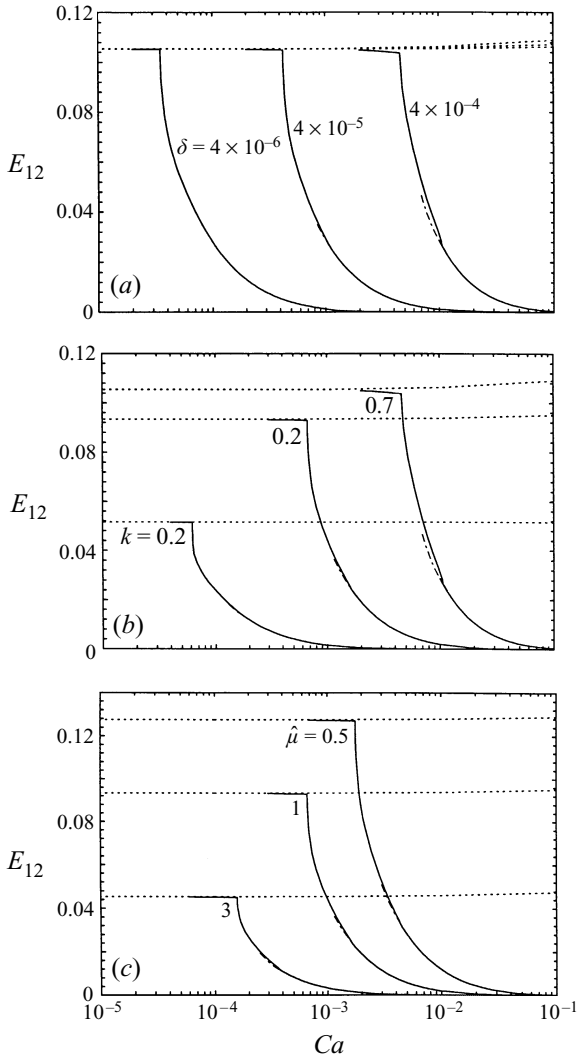

FIGURE 15. The collision efficiency for gravitational sedimentation of drops as a function of the capillary number with (*a*) $k = 0.7$, $\hat{\mu} = 1$ at $\delta = 4 \times 10^{-6}$, 4×10^{-5}, and 4×10^{-4}, (*b*) $\delta = 4 \times 10^{-4}$, $\hat{\mu} = 1$ at $k = 0.2$, 0.5, and 0.7, and (*c*) $k = 0.5$, $\delta = 4 \times 10^{-4}$ at $\hat{\mu} = 0.5$, 1, and 3. The dashed lines are for spherical drops in the presence of van der Waals forces; the solid lines are for slightly deformable drops in the presence of van der Waals forces; and the dash-dotted lines mark a discontinuity in the first derivative, neglecting the presence of the second coalescence region.

three graphs contains curves for the collision efficiency of slightly deformable drops at three values of one of the remaining three parameters, with the other two fixed. The dashed curves are for collision efficiencies of spherical drops with van der Waals forces. In each graph of figure 14, the collision efficiency for slightly deformable drops is less than that for spherical drops at lower values of δ, and then suddenly approaches the spherical drop collision efficiency at a certain δ. Figure 15 is similar to figure 14, except that the capillary number is the independent variable. In this case, at lower values of Ca, the collision efficiencies are approximately the same for slightly deformable and spherical drops, and then the two results suddenly diverge

as Ca increases, with the slightly deformable drop value asymptotically approaching zero.

In figures 14(a) and 15(a), there are three separate dashed lines for spherical drops with van der Waals attraction, which fall close together. The highest dashed line in figure 14(a) corresponds to $Ca = 0.01$ and the lowest to $Ca = 0.0001$. Similarly, in figure 15(a), the highest dashed line corresponds to $\delta = 0.0004$ and the lowest to $\delta = 4 \times 10^{-6}$. The large magnitude of the interparticle force parameter Q_{12} (see Appendix B) results in the collision efficiencies for spherical drops with molecular forces being nearly constant in the parameter range of figures 14 and 15.

Three important trends are illustrated by figures 14 and 15: first, as the viscosity ratio increases, the hydrodynamic resistance between the two drops increases, and the collision efficiency consequently decreases; second, as the size ratio increases toward unity, the relative velocity of the two drops decreases, so that they spend more time in close approach, and the collision efficiency increases; and third, as the capillary number increases, greater deformation slows down the rate of film drainage between the drops, and the collision efficiency for slightly deformable drops decreases. Furthermore, the general nature of the two figures, demonstrating a sudden change in slightly deformable drops between spherical drop behaviour and a zero asymptote in collision efficiencies, is due to the nature of the transition between rim rupture and nose rupture, as described above. The critical transition point is where multiple coalescence zones end – as indicated by an infinite slope in the lower part of the 's'-shaped curves for β_c vs. δ in figure 11. (For graphs of β_c vs. Ca, the transition point is where multiple coalescence zones begin, which would be given by an infinite slope in a now backward-'s'-shaped curve.) The presence of the second coalescence zone has a relatively small effect on the collision efficiency for $Ca \ll 1$, and it is likely that the neglected next terms in the thin-film equations for small deformations would affect the accuracy of this small correction.

The inhibiting effect of small deformation on coalescence, as exhibited in figure 15, is significant in the light of the work of Manga & Stone (1993, 1995). They found that, for air bubbles rising in corn syrup, deformation (which is relatively large in their case) actually promotes coalescence by causing alignment of the bubbles. Thus, it is possible that there is a minimum in the collision efficiency as a function of the capillary number. As explained in the Introduction, we expect that the increased coalescence displayed by deforming air bubbles in corn syrup is at least partially due to the small viscosity ratio.

Figure 16 shows the collision efficiencies for slightly deformable (solid curves) and spherical (dashed curves) drops of ethyl salicylate (ES) in diethylene glycol (DEG). The relevant physical parameters for this system (Barton & Subramanian 1989; Wang & Davis 1993) are given in table 2. This liquid pair was chosen due to its previous use in thermocapillary experiments (Barton & Subramanian 1989). To meet the assumptions underlying the model, the Reynolds number Re_2 of the larger drop and the capillary number must both be much smaller than unity. Furthermore, in the region where the transition between nose and rim rupture takes place, the Hamaker parameter δ should remain small and not exceed $O(Ca)$. In table 3, values of the three dimensionless parameters are given for $k = 0.5$ at various values of the average radius $\bar{a} = (a_1 + a_2)/2$. In order for there to be an appreciable collision efficiency, the Hamaker parameter δ should be greater than about 10^{-6}; in this range of drop sizes ($\bar{a} < 1500$ μm), the creeping flow conditions are still met.

Figure 16 indicates similar behaviour to figures 14 and 15, showing an abrupt change from spherical drop behaviour. Moreover, the collision efficiencies for spherical drops

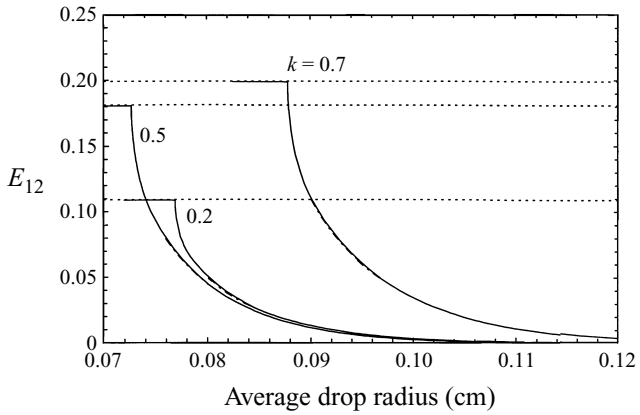

FIGURE 16. The collision efficiency for gravity-induced sedimentation of drops as a function of the average drop radius for an ES/DEG system having $\mu_e = 0.35$ g cm^{-1} s^{-1}, $\hat{\mu} = 0.1$, $\rho_e = 1.1$ g cm^{-3}, $\Delta\rho = 0.013$ g cm^{-3}, $\sigma = 1.9$ dyn cm^{-1}, and $A = 5 \times 10^{-14}$ erg for $k = 0.2$, 0.5, and 0.7. The dashed lines are for spherical drops in the presence of van der Waals forces; the solid lines are for slightly deformable drops in the presence of van der Waals forces; and the dash-dotted lines mark a discontinuity in the first derivative, neglecting the presence of the second coalescence region.

μ_e (g cm^{-1} s^{-1})	$\hat{\mu}$	ρ_e (g cm^{-3})	$\Delta\rho$ (g cm^{-3})	σ (dyn cm^{-1})	A (erg)
0.35	0.1	1.1	0.013	1.9	5×10^{-14}

TABLE 2. Data for ES/DEG system at 20°C.

$\bar{a}$ (μm)	Re_2	Ca	δ
500	1.1×10^{-2}	7.2×10^{-3}	4.7×10^{-3}
700	3.0×10^{-2}	1.4×10^{-2}	3.2×10^{-4}
900	6.4×10^{-2}	2.3×10^{-2}	4.3×10^{-5}
1100	1.2×10^{-1}	3.5×10^{-2}	8.6×10^{-6}
1400	2.4×10^{-1}	5.6×10^{-2}	1.3×10^{-6}
1600	3.6×10^{-1}	7.3×10^{-2}	4.3×10^{-7}
1700	4.3×10^{-1}	8.3×10^{-2}	2.7×10^{-7}

TABLE 3. Dimensionless groups for ES/DEG system.

with van der Waals attraction are within 0.2% of the values for spherical drops in the absence of attractive forces, again due to the magnitude of Q_{12} for the given drop sizes ($10^{10} < Q_{12} < 10^{12}$, see Appendix B). Thus, E_{12} for spherical ethyl salicylate drops sedimenting in the presence of van der Waals forces through a medium of diethylene glycol is nearly constant in the range where deformation is significant. As shown in figure 16, at a given average drop radius there is a minimum in collision efficiency versus size ratio.

The value of the average radius at which the collision efficiency for slightly deformable drops first becomes approximately equal to that for spherical drops can be estimated by using equations (3.25)–(3.29), valid for $\beta_0 \approx \pi/2$. Usually at β_c near 1.2 radians, the slope of β_c vs. average radius becomes infinite, signalling the onset of a second coalescence zone. Values of β_c in this range are at the lower limit of reliability for the $\beta \approx \pi/2$-expansion. Thus, by using the value of $\hat{\xi}_0$ which corre-

k	Equations (3.25)–(3.29)	Equations (3.13)–(3.17)	% Rel. Error
0.2	0.0776	0.0770	0.78
0.5	0.0736	0.0729	1.10
0.7	0.0890	0.0879	1.25

TABLE 4. Average radius (cm) at which $E/E_0 \sim 1$ for ES/DEG system.

sponds to $\beta_c \sim 1.2$, a first approximation can be made to the average radius at which the collision efficiencies for slightly deformable and spherical drops become nearly equal. Table 4 shows calculations for the transition point for the ES/DEG system, comparing the result from equations (3.13)–(3.17) to that from (3.25)–(3.29).

Table 3 and figure 16 can be used to estimate the range of radii for which this work is important, extending previous results for spherical drops with attractive forces. For smaller drops, molecular forces are large enough to pull the drops together before dimpling occurs, and the results for spherical drops with van der Waals forces are accurate. On the other hand, when the drop radius becomes too large, the Reynolds number increases until inertial effects can no longer be ignored.

7. Concluding remarks

Relative trajectories for two different-sized drops in buoyancy-driven motion with van der Waals forces have been calculated to determine the simultaneous effect of small deformation and short-range van der Waals forces on collision efficiencies. To satisfy the requirement that deformation be small until the drops are very close together, the capillary number is much smaller than unity. To apply the Stokes equations, the Reynolds number is also much smaller than unity. And, to keep the interfaces of the drops fully tangentially mobile, the viscosity ratio between the drops and surrounding medium is of order unity. In addition, the drop interfaces are assumed surfactant-free, and the dimensionless Hamaker constant is kept much smaller than unity to allow deformation to become important before coalescence. The main simplifications allowing an asymptotic approach to the problem are that the tangential motion of slightly deformed drops is essentially the same as that of spherical drops in close approach and that the deformation is axisymmetric. In the outer region, the spherical-drop solution is applicable and can be used to determine the driving force for the inner region, in which a lubrication regime is established.

To provide an initial gap profile for the inner region, matching arguments were used which take into account the small deviation from spherical shape that the drops would acquire prior to near contact. Results for the inner region, computed by a numerically stable semi-implicit finite difference scheme, demonstrate that the behaviour of the minimum surface clearance as a function of time is no longer symmetric and contains more than one minimum due to deformation. Moreover, in contrast to spherical drops, there are two coalescence zones over a wide range of parameter space for slightly deformable drops. This phenomenon is due to the transition from rim rupture to nose rupture when the lubrication driving force is much smaller than unity – as confirmed by an expansion of the driving force about the angle $\pi/2$ between the gravity vector and the line of centres. As demonstrated for ethyl salicylate drops in diethylene glycol, the collision efficiency of slightly deformable drops is approximately the same for spherical drops until a particular value of the average radius at which the

collision efficiencies for spherical and slightly deformed drops rapidly diverge. With a further increase in the average radii, the collision efficiency for slightly deformed drops quickly approaches zero, and the Reynolds number eventually increases beyond the Stokes flow limit. Accordingly, the average drop radii to which this analysis is applicable increases the range of drop sizes for which collision efficiencies are known, within the constraint of creeping flow.

These results confirm qualitatively the loss of symmetry of relative trajectories due to deformation observed in the experiments of Zhang *et al.* (1993). However, in order to account for other experimentally observed phenomenon, such as non-axisymmetric dimples mentioned in the concluding remarks of Yiantsios & Davis (1991), the presence of surfactants, coupled with surface tension gradients and repulsive forces, needs to be taken into account – both in asymptotic calculations and accompanying boundary-integral simulations. Most directly, however, the present work can be extended to finding collision efficiencies for slightly deformable drops in shear flow – which will result in many more possible flow patterns and a more complicated collision cross-section than the buoyancy-driven case considered here.

This work was supported by NSF Grant CTS-9416702, NASA Grant NAG3-1389, and a NASA Graduate Student Researchers Program fellowship (to M.A.R.). We are also grateful to E. J. Hinch for a discussion which has helped us to justify the approximation of axial symmetry in §3.2.

Appendix A. Collision times for spherical drops without vdW forces

The collision times for spherical drops without van der Waals attraction, acting under the influence of a constant driving force (3.23) and a linearly varying driving force (3.31), are based on previous work (Davis *et al.* 1989; Zinchenko 1982) for the motion of two spherical drops in close approach. The hydrodynamic lubrication force F is given by

$$F = -6\pi\mu_e a_1 \Lambda_{11} W, \tag{A 1}$$

where W is the relative velocity of the two drops and Λ_{11} is given by the first term of the asymptotic expansion (2.1) of Zinchenko (1982). Substituting $\mathrm{d}h_0/\mathrm{d}t$ for W and the expression for Λ_{11} into (A 1) gives

$$F = -\tfrac{3}{8}\sqrt{2}\,\pi^3\mu'\left(\frac{a_1 a_2}{a_1 + a_2}\right)^{3/2}\frac{1}{h_0^{1/2}}\frac{\mathrm{d}h_0}{\mathrm{d}t}. \tag{A 2}$$

When F is constant and set equal to (3.2) with $\beta = \beta_0$, and the variables are made dimensionless according to (3.12), the differential equation (A 2) can be recast as (with the tildes dropped from the dimensionless variables)

$$-\tfrac{3}{16}\sqrt{2}\,\pi^2\frac{\mathrm{d}h_0}{h_0^{1/2}} = \alpha\cos\beta_0\,\mathrm{d}t, \tag{A 3}$$

where α is defined by (3.19). Integration from h_0 at $t = 0$ to $h_0 = 0$ at $t = t_{coll}$ then yields (3.23) for t_{coll} as a function of h_0.

When F varies linearly with time as given by the right-hand side of (3.29), and the variables are made dimensionless with (3.12) and (3.24), then (A 2) becomes

$$-\tfrac{3}{16}\sqrt{2}\,\pi^2\frac{\mathrm{d}\hat{h}_0}{\hat{h}_0^{1/2}} = (\hat{\xi}_0 - \hat{t})\mathrm{d}\hat{t}. \tag{A 4}$$

Subsequent integration of (A4) from $\hat{h}_0$ at $\hat{t} = 0$ to $\hat{h}_0 = 0$ at $\hat{t} = \hat{t}_{coll}$ provides the result (3.31), when the physically meaningful root is taken from the quadratic equation.

Appendix B. Collision efficiencies of spherical drops with vdW attraction

The procedure of Zhang & Davis (1991) was used to determine the collision efficiencies for spherical drops with van der Waals forces for comparison with the slightly deformable drop results. The trajectory equation for spherical drops with interparticle forces is (Zhang & Davis 1991; Zinchenko & Davis 1994)

$$\frac{\mathrm{d}s}{\mathrm{d}\beta} = s\,\frac{-\left(L(s)\cos\beta + \dfrac{G(s)}{Q_{12}}\,\dfrac{\mathrm{d}\phi_{12}}{\mathrm{d}s}\right)}{M(s)\sin\beta}. \tag{B 1}$$

Here, s, L, and M are the same as in (6.1)–(6.4). In addition, G is the relative mobility function for spherical drop motion due to an equal and opposite force along the line of centres (Haber *et al.* 1973); $\mathrm{d}\phi_{12}/\mathrm{d}s$ is the dimensionless gradient of the interparticle potential scaled with the Hamaker constant A, and Q_{12} is the dimensionless interparticle force parameter:

$$Q_{12} = \tfrac{2}{3}\,\frac{\pi a_1 a_2 (a_2^2 - a_1^2)\Delta\rho g}{A}. \tag{B 2}$$

When Q_{12} is large, the effect of interparticle forces is small except for drops in very close approach.

The dimensionless critical impact parameter was calculated by trial and error from equation (B 1) to locate the trajectory where the van der Waals force balances the gravitational force at $\beta = \pi$. Numerically, this scheme required systematically varying the matching angle, β_f, at a matching separation, s_f, of 9.0, chosen so that molecular forces are negligible, and integrating forward with the fourth-order Runge–Kutta method. Once the limiting condition, β_f, is specified, the collision efficiency, E_{12}, is found by

$$E_{12} = \tfrac{1}{4}\,y_c^2 = \frac{1}{4}\left[s_f \sin\beta_f \exp\left(\int_{s_f}^{\infty} \frac{L - M}{sL}\,\mathrm{d}s\right)\right]^2. \tag{B 3}$$

The value of the integral on the right-hand side of equation (B3) can be provided analytically from the far-field expansions for L and M. The results for L, M, and G were verified with figures 1 to 7 of Zhang & Davis (1991), while the values for E_{12} matched well with those from figure 19 of the same paper.

To compare results for slightly deformable drops with those for spherical drops sedimenting in the presence of molecular forces, equivalence was established between the dimensionless interparticle force parameter, Q_{12}, and the dimensionless variables used in the slightly deformable drop analysis. Some manipulation reveals that

$$Q_{12} = \left(\frac{2\pi}{9}\right)^3 \frac{(1-k)^3(k+1)^{11}}{k^7} \left(\frac{\hat{\mu}+1}{\hat{\mu}+\frac{2}{3}}\right)^2 \frac{1}{Ca^2\,\delta}. \tag{B 4}$$

In table 5, some typical values of E_{12} are given for spherical drops with van der Waals forces for $k = 0.7$ and $\hat{\mu} = 1$ at various locations in dimensionless parameter space for slightly deformable drops where deformation is important. Note that the value of E_{12} at the given size and viscosity ratio is 0.1053 for spherical drops without van der Waals forces. For typical values of δ and Ca where deformation is important,

Ca	δ	Q_{12}	E_{12}
0.1	0.0004	1.376×10^{7}	0.1090
0.1	0.00004	1.376×10^{8}	0.1073
0.01	0.0004	1.376×10^{9}	0.1062
0.01	0.00004	1.376×10^{10}	0.1058
0.001	0.0004	1.376×10^{11}	0.1054

TABLE 5. E_{12} with vdW at various Ca and δ.

Q_{12} is commonly of the order of 10^{10}, and E_{12} for spherical drops with van der Waals forces is within 0.5% of E_{12} for spherical drops without van der Waals forces. The largest deviation in table 5 from E_{12} without attractive forces is 3.5%.

REFERENCES

BARTON, K. & SUBRAMANIAN, R. 1989 The migration of liquid drops in a vertical temperature gradient. *J. Colloid Interface Sci.* **133**, 211–222.

BENTLEY, B. G. & LEAL, L. G. 1986 An experimental investigation of drop deformation and breakup in steady two-dimensional linear flows. *J. Fluid Mech.* **167**, 241–283.

CHESTERS, A. K. 1991 The modelling of coalescence processes in fluid-fluid dispersions, A review of current understanding. *Trans. Inst. Chem. Engrs* **69**, 259–270.

COLE, J. 1968 *Perturbation Methods in Applied Mathematics*. Ginn-Blaisdell.

COOLEY, M. D. A. & O'NEILL, M. E. 1969 On the slow motion generated in a viscous fluid by the approach of a sphere to a plane wall or stationary sphere. *Mathematika* **16**, 37–49.

DAVIS, R. H., SCHONBERG, J. A. & RALLISON, J. M. 1989 The lubrication force between two viscous drops. *Phys. Fluids* A **1**, 77–81.

DAVIS, R. H., SERAYSSOL, J. & HINCH, E. J. 1986 The elastohydrodynamic collision of two spheres. *J. Fluid Mech.* **163**, 479–497.

DERJAGUIN, B. & KUSSAKOV, M. 1939 Anomalous properties of thin poly-molecular films. *Acta Physicochim. URSS* **10**, 25–30.

FUENTES, Y. O., KIM, S. & JEFFREY, D. J. 1988 Mobility functions for two unequal viscous drops in Stokes flow. I. Axisymmetric motions. *Phys. Fluids* **31**, 2445–2455.

FUENTES, Y. O., KIM, S. & JEFFREY, D. J. 1989 Mobility functions for two unequal viscous drops in Stokes flow. II. Non-axisymmetric motions. *Phys. Fluids* A **1**, 61–76.

HABER, S., HESTRONI, G. & SOLAN, A. 1973 On the low Reynolds number motion of two droplets. *Intl J. Multiphase Flow* **1**, 57–71.

HAGEMAN, A. & YOUNG, M. 1981 *Applied Iterative Methods*. Academic.

HAHN, P. S., CHEN, J.-D. & SLATTERY, J. C. 1985 Effects of London–van der Waals forces on the thinning and rupture of a dimpled liquid film as a small drop or bubble approaches a fluid-fluid interface. *AIChE J.* **31**, 2026–2038.

HAMAKER, H. C. 1937 The London-van der Waals attraction between spherical particles. *Physica* **4**, 1058–1072.

JONES, A. F. & WILSON, S. D. R. 1978 The film drainage problem in droplet coalescence. *J. Fluid Mech.* **87**, 263–288.

MANGA, M. H. & STONE, H. A. 1993 Buoyancy-driven interactions between two deformable viscous drops. *J. Fluid Mech.* **256**, 647–683.

MANGA, M. H. & STONE, H. A. 1995 Collective hydrodynamics of deformable drops and bubbles in dilute low Reynolds number suspensions. *J. Fluid Mech.* **300**, 231–263.

O'NEILL, M. E. & STEWARTSON, K. J. 1967 On the slow motion of a sphere parallel to a nearby plane wall. *J. Fluid Mech.* **27**, 705–710.

RALLISON, J. M. 1984 The deformation of small viscous drops and bubbles in shear flows. *Ann. Rev. Fluid Mech.* **16**, 45–66.

REDDY, S. R., MELIK, D. H. & FOGLER, H. S. 1981 Emulsion stability-theoretical studies on simultaneous flocculation and creaming. *J. Colloid Interface Sci.* **82**, 116–127.

Reed, L. D. & Morrison, F. A. 1974 The slow motion of two touching fluid spheres along their line of centres. *Intl J. Multiphase Flow* **1**, 573–583.

Rogers, J. R. & Davis, R. H. 1990 Modelling of collision and coalescence of droplets during microgravity processing of Zn-Bi immiscible alloys. *Metall. Trans.* **21A**, 59–68.

Rushton, E. & Davies, G. A. 1978 The slow motion of two spherical particles along their line of centres. *Intl J. Multiphase Flow* **4**, 357–381.

Saboni, A., Gourdon, C. & Chesters, A. K. 1995 Drainage and rupture of partially mobile films during coalescence in liquid-liquid systems under a constant interaction force. *J. Colloid Interface Sci.* **175**, 27–35.

Wang, H. & Davis, R. H. 1993 Droplet growth due to Brownian, gravitational, or thermocapillary motion & coalescence in dilute dispersions. *J. Colloid Interface Sci.* **159**, 108–118.

Wang, H. & Davis, R. H. 1995 Simultaneous sedimentation and coalescence of a dilute dispersion of small drops. *J. Fluid Mech.* **295**, 247–261.

Wang, H., Zinchenko, A. Z. & Davis, R. H. 1994 The collision rate of small drops in linear flow fields. *J. Fluid Mech.* **265**, 161–188.

Yiantsios, S. G. & Davis, R. H. 1990 On the buoyancy-driven motion of a drop towards a rigid surface or a deformable interface. *J. Fluid Mech.* **217**, 547–573.

Yiantsios, S. G. & Davis, R. H. 1991 Close approach and deformation of two viscous drops due to gravity and van der Waals forces. *J. Colloid Interface Sci.* **144**, 412–433.

Yiantsios, S. G. & Higgins, B. G. 1989 Rayleigh–Taylor instability in thin viscous films. *Phys. Fluids* A **1**, 1484–1501.

Zhang, X. & Davis, R. H. 1991 The rate of collisions of small drops due to Brownian or gravitational motion. *J. Fluid Mech.* **230**, 479–504.

Zhang, X., Davis, R. H. & Ruth, M. F. 1993 Experimental study of two interacting drops in an immiscible fluid. *J. Fluid Mech.* **249**, 227–239.

Zhang, X., Wang, H. & Davis, R. H. 1993 Collective effects of temperature gradients and gravity on droplet coalescence. *Phys. Fluids* A **5**, 1602–1613.

Zinchenko, A. Z. 1978 Calculation of hydrodynamic interactions between drops at low Reynolds number. *Prikl. Mat. Mech.* **42**, 1046–1051.

Zinchenko, A. Z. 1980 The slow asymmetrical motion of two drops in a viscous medium. *Prikl. Mat. Mech.* **44**, 30–37.

Zinchenko, A. Z. 1982 Calculations of the effectiveness of gravitational coagulation of drops with allowance for internal circulation. *Prikl. Mat. Mech.* **46**, 58–65.

Zinchenko, A. Z. 1994 Algorithm for random close packing of spheres with periodic boundary conditions. *J. Comput. Phys.* **114**, 298–307.

Zinchenko, A. Z. & Davis, R. H. 1994 Gravity-induced coalescence of drops at arbitrary Peclet numbers. *J. Fluid Mech.* **280**, 119–148.

Zinchenko, A. Z. & Davis, R. H. 1995 Collision rates of spherical drops or particles in a shear flow at arbitrary Peclet numbers. *Phys. Fluids* **7**, 2310–2327.

Zinchenko, A. Z., Rother, M. A. & Davis, R. H. 1997 A novel boundary-integral algorithm for viscous interaction of deformable drops. *Phys. Fluids* **9**, 1493–1511.